



GEORG-AUGUST-UNIVERSITÄT  
GÖTTINGEN

Fakultät für  
Physik 

## Master's Thesis

# Vorbereitende Datenanalyse zur Rekonstruktion von Echtzeit-MRT-Daten

## Preparatory data analysis for the reconstruction of real-time MRI data

prepared by

**Hans Christian Martin Holme**

from Soest

at the Biomedizinische NMR Forschungs GmbH  
am Max-Planck-Institut für biophysikalische Chemie



**Date of Submission:** 18th February 2016

**First Referee:** Prof. Dr. Jens Frahm

**Second Referee:** Prof. Dr. Tim Salditt



# Contents

<b>1. Introduction</b>	<b>1</b>
<b>2. Magnetic Resonance and Image Reconstruction</b>	<b>3</b>
2.1. Magnetic Resonance Imaging . . . . .	3
2.1.1. Principles . . . . .	3
2.1.2. Radial FLASH . . . . .	8
2.2. Non-linear Inverse Reconstruction . . . . .	11
2.3. Undersampling and Image Artifacts . . . . .	12
<b>3. Methods</b>	<b>15</b>
3.1. Data Acquisition and Processing . . . . .	15
3.1.1. Pre- and Postprocessing . . . . .	16
3.1.2. nlinv++ . . . . .	16
3.2. Data Visualization . . . . .	18
<b>4. Coil Compression</b>	<b>21</b>
4.1. Principal Component Analysis . . . . .	21
4.1.1. The PCA Algorithm . . . . .	21
4.1.2. Application in real-time MRI . . . . .	22
4.2. Optimized Combination . . . . .	25
4.3. Performance Evaluation . . . . .	30
4.4. Discussion . . . . .	36
<b>5. Coil Selection</b>	<b>37</b>
5.1. Current Methods . . . . .	41
5.1.1. Manual Selection . . . . .	41
5.1.2. Xue et al. . . . .	41
5.1.3. Grimm et al. . . . .	42
5.2. Sinogram-based Selection . . . . .	47
5.3. Discussion . . . . .	54

## *Contents*

<b>6. Summary and Outlook</b>	<b>55</b>
<b>A. Additional Figures</b>	<b>57</b>
<b>B. Sequence Parameters</b>	<b>61</b>
<b>Bibliography</b>	<b>63</b>

# Glossary

CT	computed tomography
DFT	discrete Fourier transform
FID	free induction decay
FLASH	fast low-angle shot
FOV	field of view
GPU	graphics processing unit
GRAPPA	generalized autocalibrating partially parallel acquisition
IRGNM	iteratively regularized Gauss-Newton method
MRI	magnetic resonance imaging
NLINV	non-linear inverse reconstruction
NMR	nuclear magnetic resonance
PCA	principal component analysis
PSF	point spread function
rf	radio frequency
SENSE	sensitivity encoding
SNR	signal-to-noise ratio
$T_1$	spin-lattice relaxation time

## *Glossary*

$T_2$  . . . . . spin-spin relaxation time

$T_2^*$  . . . . . effective spin-spin relaxation time

# 1. Introduction

Magnetic resonance imaging (MRI) is an important radiological technique for imaging sections or volumes in clinical and scientific settings. Starting from its introduction by Lauterbur [1] in 1973, it has evolved into a routine procedure. Because of the lack of ionizing radiation, its excellent soft tissue contrast, and its wide variety of imaging modalities, it is now used in hospitals and research institutes worldwide.

An inherent problem of MRI is its low speed, since images are sampled line-by-line in Fourier space. This low inherent speed has practical implications, e.g. movement during the acquisitions degrades image quality, and dynamical processes impose requirements on image timing. Therefore, acceleration of MRI image acquisition has been a research focus since its beginning.

A success in this drive for speed has been the introduction of fast low-angle shot (FLASH) imaging in 1985[2–4], which reduced the imaging time from minutes to mere seconds. This hastened the integration of MRI into routine clinical use. Further speed improvements based on FLASH MRI were possible by tackling the sampling: The introduction of multiple receiver coils, combined with parallel MRI [5], allows image reconstruction even from undersampled data. Pushing this undersampling further leads to the common trade-off of increased imaging speed at the cost of decreased signal-to-noise ratio (SNR).

Nowadays, accelerated acquisition sequences coupled with sophisticated reconstruction algorithms to cope with the high undersampling have pushed this even further, with imaging times below 30 ms [6]. This enables the recording of MRI movies instead of still images. Together with modern computer hardware, this led to the introduction of real-time MRI, with both image acquisition and image reconstruction in real time.

While holding great promise, real-time MRI also poses new challenges: The increased imaging speeds, for example, lead to large volumes of data which, together with computationally intensive reconstruction algorithms, can diminish reconstruction speeds. Furthermore, the high degree of undersampling can lead to unacceptable image artifacts. This thesis introduces and evaluates approaches for handling these two problems. Chapter 4 discusses coil compression methods for reducing the data volume, while a new coil selection algorithm for streak artifact reduction is introduced in Chapter 5.





## 2. Magnetic Resonance and Image Reconstruction

This chapter provides a brief overview over nuclear magnetic resonance (NMR) and MRI, and also an introduction into the reconstruction technique used in this work. A more general introduction into MRI and the underlying physics is given in textbooks like Bernstein, King, and Zhou [7] and Haacke et al. [8].

### 2.1. Magnetic Resonance Imaging

#### 2.1.1. Principles

This section follows Chapters 1 and 9 of Haacke et al. [8].

MRI relies on the interaction of a magnetic moment  $\mu$  with an external field  $B_0$ . The magnetic moment in this case is the nuclear magnetic moment, generated by the nuclear spin. The principal nucleus used in MRI is hydrogen in water, fat, and other organic molecules.

For a hydrogen nucleus — a proton — in a magnetic field  $B_0$ , the Zeeman effect leads to an energy difference between parallel and anti-parallel alignment of the spin, with alignment parallel to  $B_0$  having lower energy. The energy difference is  $\hbar\gamma B_0$ , where  $\hbar$  is the reduced Planck constant and  $\gamma$  is the gyromagnetic ratio, a nucleus-dependent value.

While this constrains the nuclear magnetic moment in the direction of  $B_0$  to two possible values, there is no such restriction in the transversal plane orthogonal to  $B_0$ . Therefore, in analogy to a classical magnetic moment, the expectation value will start to precess around  $B_0$ . The frequency of this precession is called the Larmor frequency  $\omega_0$  with  $\omega_0 = \gamma B_0$ . In an extended object made up of multiple spins, since there is no phase coherence imposed on this precession, the transversal magnetic moments cancel out, leaving a bulk magnetization parallel to  $B_0$ .

Since the energy difference between alignment parallel and anti-parallel to  $B_0$  is small compared to the thermal energy at body temperature, the population difference between

## 2. Magnetic Resonance and Image Reconstruction

the two states is also small — at 1 T, the population difference is about 6 excess spins per million [9, p. 36] — but it still leads to a macroscopic magnetization  $M_0$  which is large enough for NMR effects.  $M_0$  is given by [8, p. 5]  $M_0 = \frac{\rho_0 \gamma^2 \hbar^2}{4kT} B_0$ , where  $\rho_0$  is the number of protons per unit volume,  $k$  is the Boltzmann constant, and  $T$  is the temperature.

Precession of the macroscopic magnetization can be achieved by resonant excitation. The resonance condition is that the frequency of the magnetic excitation pulse  $B_1(t)$  needs to be the Larmor frequency. For the commonly used nuclei and field strengths this frequency is in the radio-frequency range, the excitation pulses are therefore commonly called radio frequency (rf) pulses. The angle by which the magnetization is tipped is called the flip angle, and it depends both on the field strength and duration of the rf pulse. The excitation pulse achieves its effect by two mechanisms: First, it will flip spins from the lower energy parallel to the higher energy anti-parallel state, thereby reducing longitudinal magnetization. Second, it will impose its phase onto the precession, thereby causing a non-vanishing transversal magnetization. Combined, this leads to a bulk magnetization that starts to precess and to tip over the duration of the rf pulse.

Suppose an rf pulse is applied that tips the magnetization into the transversal plane (called a  $90^\circ$ -pulse). Directly after this pulse, the bulk magnetization precesses in the transversal plane. This magnetization will induce a changing magnetic flux in nearby coils, which can be detected.

The longitudinal magnetization will eventually relax back into the equilibrium state. This can be understood as the spins excited into the anti-parallel state flipping back into the parallel state. This is an exponential process characterized by the spin-lattice relaxation time ( $T_1$ ). If the equilibrium magnetization is  $M_0$ , the longitudinal magnetization will recover according to:

$$M_{\parallel}(t) = M_0 \left( 1 - e^{-\frac{t}{T_1}} \right).$$

Furthermore, the different spins are not only affected by the external magnetic field, but also by the magnetic fields produced by other spins. This leads to slightly different Larmor frequencies for each spin, causing a loss of phase coherence called dephasing and thereby a loss of bulk transversal magnetization. This decay is characterized by the spin-spin relaxation time ( $T_2$ ), following

$$M_{\perp}(t) = M_0 e^{-\frac{t}{T_2}}.$$

$T_2$  is always shorter than  $T_1$ , with typical values for  $T_2$  on the order of 1 ms to 100 ms and for  $T_1$  on the order of 100 ms to 1000 ms. Inhomogeneities of the static magnetic field  $B_0$  will lead to even faster dephasing, characterized by the effective spin-spin relaxation time ( $T_2^*$ ) with  $T_2^* < T_2$ .

Application of an excitation pulse to an object generates a decaying signal called free induction decay (FID). An alternative way to create a signal is by generating an echo. The basic setup is the same: a  $90^\circ$ -pulse is applied to tip the magnetization into the transversal plane, where they will dephase due to  $T_2$  decay. By applying a second rf-pulse after  $\tau$ , this time a  $180^\circ$ -pulse, the magnetization stays in the transversal plane but it is rotated by  $180^\circ$  about an axis within the transversal plane; or alternatively, the phase of each spin is turned to its negative. This means that the spins that acquired excess phase between excitation and  $180^\circ$ -pulse now lag behind and vice versa. Therefore, the spins rephase at  $t = 2\tau$  and an echo forms. This is called a spin echo. The strength is still attenuated by  $e^{-2\tau/T_2}$  due to  $T_2$  decay. Figure 2.1a shows a diagram of spin echo formation.

An echo can also be generated without using a second rf pulse. For this, the spins are first dephased by applying a gradient and then rephased by applying a gradient with the same strength but with the opposite sign. The echo is formed at the instant where the combined area under both gradients equals zero. The resulting echo is called a gradient echo or gradient-recalled echo. In contrast to a spin echo, the gradient echo is attenuated by the shorter  $T_2^*$ , since the magnetic field inhomogeneities are not canceled out by phase inversion. Figure 2.1b depicts gradient echo formation.

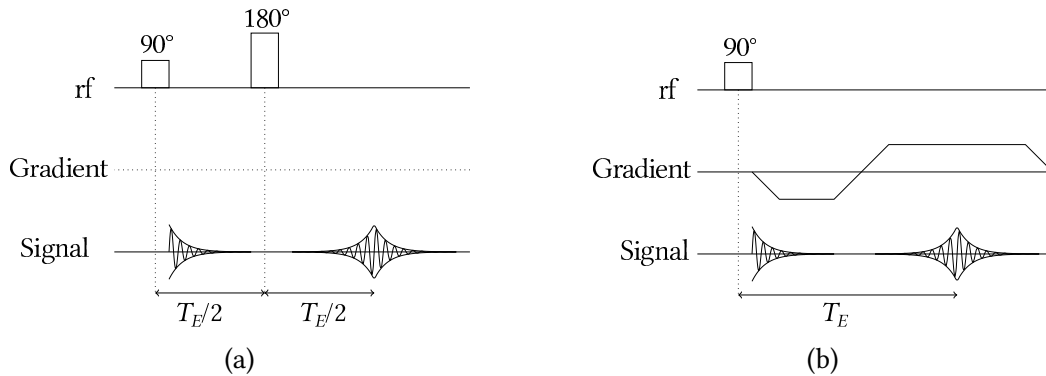


Figure 2.1: Diagram for (a) spin echo and (b) gradient echo formation. For the spin echo in (a), no gradients are necessary: after an initial  $90^\circ$  rf-pulse, the FID signal begins to decay. Applying a  $180^\circ$ -pulse after  $T_E/2$  leads to a spin echo after  $T_E$ . The gradient echo in (b) shows the same FID decay after the  $90^\circ$ -pulse, but the spins are then dephased and rephased with an applied gradient. Plotted here is the gradient strength over time. Diagrams adapted from [10].

For generating an image, it is necessary to relate spatial position and signal. The idea in MRI is to use magnetic gradient fields and exploit the linear dependence of the Larmor frequency on field strength. This can be understood most easily in the one-dimensional

case: By applying a linear gradient  $G(t)$  in  $x$ -direction the total magnetic field becomes  $B(x,t) = B_0 + xG(t)$ . This changes the local Larmor frequency to  $\omega(x,t) = \omega_0 + \Delta\omega(x,t)$  with  $\Delta\omega(x,t) = \gamma xG(t)$ . This is called frequency encoding, since the position of the spins is hereby related to their precession frequency. The signal  $s(t)$  in MRI depends on the effective spin density<sup>1</sup>  $\rho(\mathbf{r})$  and the phase of the precessing spins  $\phi(\mathbf{r},t)$  [8, p. 141],

$$s(t) = \int \rho(\mathbf{r}) e^{i(\omega_0 t + \phi(\mathbf{r},t))} d^3r$$

where  $\phi(\mathbf{r},t) = -\int_0^t \omega(\mathbf{r},t) dt$ . For a one-dimensional object  $\rho(\mathbf{r}) = \rho(x)\delta(y)\delta(z)$ , the signal after frequency encoding and demodulation of  $\omega_0$  becomes

$$s(t) = \int \rho(x) e^{-i \int_0^t \Delta\omega(x,t) dt} dx.$$

By noting that  $\int_0^t \Delta\omega(x,t) dt = \gamma x \int_0^t G(t) dt$  and introducing  $2\pi k(t) := \gamma \int_0^t G(t) dt$ , the time dependence can be made implicit in  $k$ :

$$s(k) = \int \rho(x) e^{-2\pi i k x} dx.$$

Here,  $s(k)$  is the Fourier transform of  $\rho(x)$ , and so can be inverted to obtain the spin density from a frequency-encoded measurement  $\rho(x) = \int s(k) e^{2\pi i k x} dx$ . The  $k$  is naturally identified as a vector in the reciprocal or Fourier space, called  $k$ -space in MRI. The temporal evolution of the gradient determines  $k(t)$ , which is referred to as the trajectory in  $k$ -space. In practice, the signal cannot be recorded continuously but is sampled at discrete points instead.

The gradient echo introduced above is an example of a trajectory that can be used to sample a region around the center of  $k$ -space: The first dephasing gradient moves the sampling point away from the  $k$ -space center for a time  $\tau$ . If the subsequent rephasing gradient has the same gradient strength but twice the duration, a symmetric line around the  $k$ -space center will be encoded in the signal. If it is sampled during the rephasing gradient, this symmetric  $k$ -space line can be used to reconstruct the object by 1D Fourier transformation.

For two-dimensional objects, there are several encoding schemes. One is radial encoding, which will be explained in Section 2.1.2, another is Cartesian encoding. For Cartesian encoding, parallel lines are sampled in  $k$ -space. Each line of  $k$ -space is measured with frequency encoding in a separate repetition, so with a separate excitation pulse. To measure shifted lines in  $k$ -space an additional gradient, called phase-encoding gradient, is applied between excitation and frequency encoding. The direction of this gradient has

---

<sup>1</sup>The effective spin density is the plain spin density  $\rho_0$  with all constants absorbed into it. This simplifies the resulting expressions. See p. 141 of Haacke et al. [8] for an exact definition.

to be orthogonal to the frequency-encoding direction. This gradient leads to a phase shift in real space, which in turn implies a translation in  $k$ -space. For a certain choice of line separation, gradient strength and sampling rate, the measured samples will lie on a Cartesian grid in  $k$ -space, hence the name Cartesian encoding. The reconstruction is simply a two-dimensional discrete Fourier transform. Figure 2.2a shows a diagram of a Cartesian encoding scheme.

For imaging a slice of a three-dimensional object, slice selection can be used. Here, a gradient orthogonal to the desired slice is applied during the excitation pulse. If the gradient is such that it is zero in the desired slice, the Larmor frequency changes everywhere except in the slice itself, so the resonance condition is only fulfilled in the slice and only it will be excited, yielding effectively a two-dimensional object for imaging.

For three-dimensional imaging, either phase encoding can be extended in the third direction, or slice selection can be used to image each slice serially.

Image reconstruction in MRI invariably involves discretization, which introduces the problem of sampling: the imaging procedures described above can only work if proper sampling is taken into account, with the sampling rate subject to the Nyquist criterion and the maximum  $k$ -space extent determining the resolution [8, Ch. 12]. Sampling and associated artifacts are discussed in more detail in Section 2.3.

In general, the choice and timing of imaging gradients and rf pulses can modify the contrast of MRI images to an astonishing degree, with far more possibilities than could be described here. An overview over a large number of MRI sequences can be found in Bernstein, King, and Zhou [7].

Modern MRI uses multiple receive coils. An advantage is the increased signal-to-noise ratio (SNR), which comes from smaller coils which can be placed closer to the object. Multiple coils with overlapping sensitivity profiles can cover the same volume as a single large coil. But, instead of the single global image reconstructed above, each coil contains information from only part of the object. Therefore, a combined image is normally calculated as the root-sum-of-squares of the individual coil images [11]. A further advantage of multiple receive coils is the possibility of parallel imaging: 2D and especially 3D images require a large number of repetitions, leading to long measurement times. The idea of parallel imaging is to speedup this process by using the spatial information contained in the sensitivity variation of the coils to replace time-consuming spatial encoding.

In Cartesian imaging, the speedup comes from skipping phase-encoding lines. This leads to reduced coverage of  $k$ -space called undersampling. Special reconstruction techniques are necessary to recover usable images, since naive Fourier reconstruction with skipped phase-encoding lines leads to aliasing in the images. Common parallel imaging techniques

include sensitivity encoding (SENSE)[12], generalized autocalibrating partially parallel acquisition (GRAPPA)[13], and the non-linear inverse reconstruction (NLINV) used in this thesis and described in Section 2.2. An overview over parallel imaging techniques can be found in Deshmane et al. [5].

### 2.1.2. Radial FLASH

#### FLASH

The most important pulse sequence in this thesis is radial fast low-angle shot (FLASH). FLASH is a technique for rapid acquisition of MRI images, introduced in 1985 by Frahm et al. [2]. The acquisition scheme described above uses  $90^\circ$ -pulses, which maximizes the usable transversal magnetization for imaging, but also necessitates waiting for full  $T_1$  recovery before the next excitation. FLASH uses gradient echoes and small angle pulses with flip angles smaller than  $15^\circ$ . Combined with continuous imaging, this leads to the development of a steady state, with the longitudinal magnetization lost to rf excitation being recovered through  $T_1$  relaxation during the sequence. With continuous imaging, even the transverse phase coherence does not relax completely. This needs to be rectified, either by applying strong gradients, called crusher gradients, which completely dephase the transverse magnetization; or by rf-spoiling, which applies a phase offset onto each excitation pulse, thereby suppressing the buildup of a steady state of the transversal magnetization [8, p. 500f]. For fast imaging, rf spoiling is preferred, since it avoids the time-consuming crusher gradients. With rf-spoiled FLASH, repetition times on the order of 2 ms are possible. The steady state which is built up during a FLASH acquisition also dictates the contrast: Since this steady state is  $T_1$ -dependent, FLASH-acquisitions with short repetition times and short echo times on the order of milliseconds, like the sequences used for real-time MRI, will show  $T_1$ -weighting, with shorter  $T_1$  appearing brighter.

#### Radial Imaging

Radial encoding is the other difference to current routine MRI. Instead of recording lines on a Cartesian grid in  $k$ -space, lines through the  $k$ -space center are recorded in a pattern similar to spokes on a wheel. While it is not necessary, the radial trajectories in this thesis use equiangular spacing. A diagram of a radial trajectory is shown in Figure 2.2b. It is immediately obvious that radial trajectories sample  $k$ -space non-uniformly. This is a problem in the outer regions of  $k$ -space which contain high resolution information:

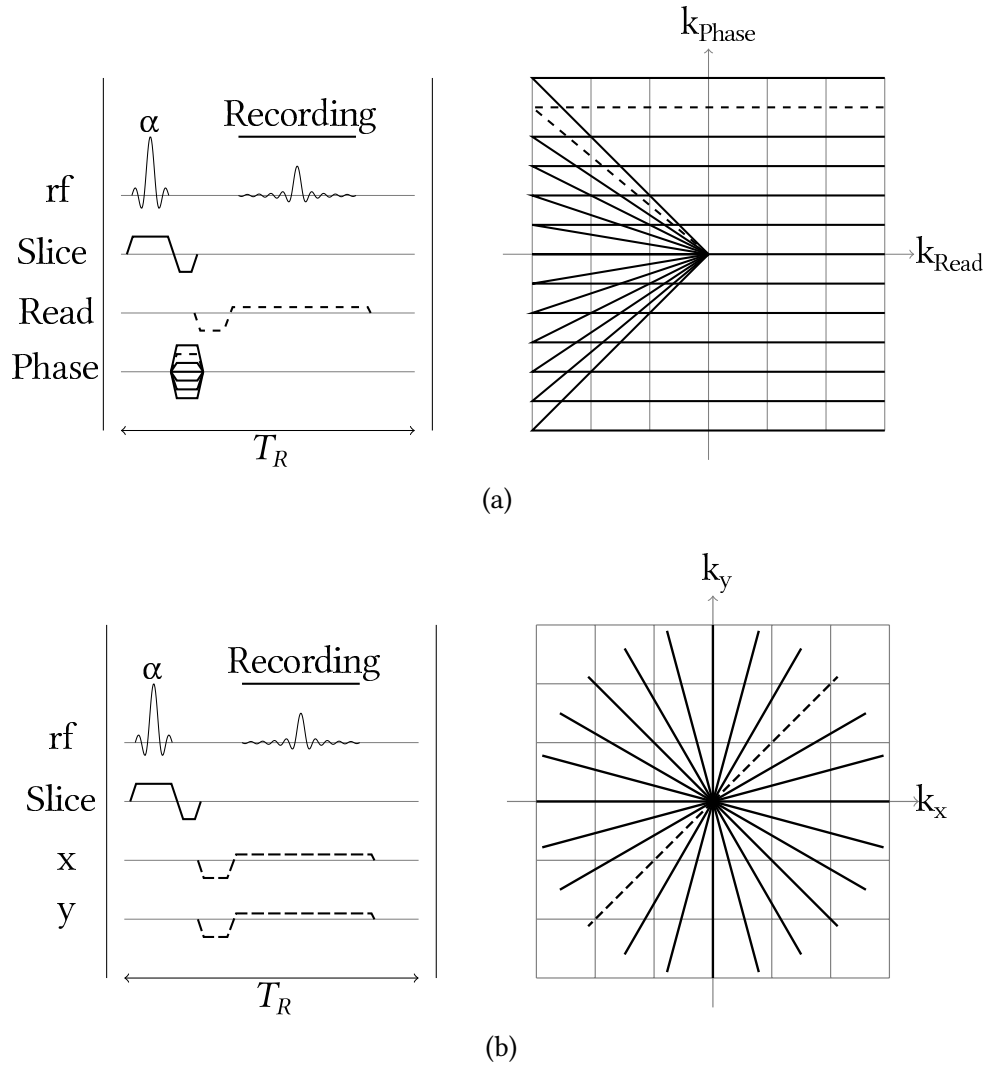


Figure 2.2: Sequence and  $k$ -space diagrams for (a) Cartesian and (b) radial encoding. The dashed gradient line in the sequence diagram corresponds to the dashed  $k$ -space line in the  $k$ -space diagram. Both contain an  $\alpha$ -pulse and a slice selection gradient. In (a) Cartesian encoding, the same frequency-encoding gradient is used during readout in all lines, only the phase-encoding gradient changes. In (b) radial encoding, both  $x$  and  $y$  gradients use frequency encoding, so both are present during readout. Diagrams adapted from [10].

## 2. Magnetic Resonance and Image Reconstruction

The lower sampling in this region means that radial trajectories need to measure more lines to achieve similar resolution to Cartesian trajectories. The higher sampling of  $k$ -space close to the center, however, is an advantage over Cartesian imaging, since it leads to reduced motion sensitivity. Another advantage is the absence of a phase-encoding gradient, enabling shorter echo times and, together with FLASH, faster repetition rates.

Radial imaging also allows uniform readout oversampling. This means faster sampling of the MRI signal, commonly doubling the sampling rate, thereby enlarging the field of view (FOV) without affecting the resolution. The aliasing artifacts arising from discrete and finite sampling of  $k$ -space are hereby moved further from the region of interest. After reconstruction, the excess part of the FOV is discarded again. Since it is done during sampling, no additional imaging time is needed, and while readout oversampling is limited to the frequency-encoding direction in Cartesian imaging, no such limitation exists in radial imaging.

Reconstruction also changes with radial encoding: A simple inverse 2D Fourier transform is no longer possible. Instead, there are two main ways to reconstruct images: Projection reconstruction and gridding. Projection reconstruction relies on the Fourier slice theorem, which states that the 1D Fourier transform of lines through the origin of  $k$ -space are the projections orthogonal to the line. With this, each measured line can be Fourier transformed, mapped to an angle, and then reconstructed with methods like filtered backprojection or other techniques common in computed tomography (CT). Gridding is an alternative approach, where the radial spokes are resampled onto a Cartesian grid, which is then 2D Fourier transformed.

The most important advantage of radial trajectories is, however, the possibility of uniform (azimuthal) undersampling: In Cartesian MRI, only the phase-encoding direction can be undersampled reasonably; undersampling the frequency-encoding direction does not lead to an appreciable decrease in measurement time. But the non-uniform sampling achieved by skipping phase-encoding lines limits the degree of undersampling that can be used. With radial sampling, since each spoke samples both low and high  $k$ -space regions, measuring fewer spokes while retaining equiangular spacing leads to uniform undersampling. For real-time MRI, where very high undersampling factors are used, this uniform undersampling also helps with temporal resolution: In Cartesian MRI, the central  $k$ -space which contains overall object shape is only measured once per frame. In radial acquisition, each spoke measures the  $k$ -space center, so each spoke contains equally important data. Undersampling and related image artifacts is described in more detail in Section 2.3. The application of radial FLASH for real-time MRI is described, for example, in Zhang, Block, and Frahm [14] and Uecker et al. [6].



## 2.2. Non-linear Inverse Reconstruction

The most important ingredient for real-time MRI is the non-linear inverse reconstruction (NLINV) introduced by Uecker et al. [15] in 2008.

A closer look at the signal in parallel MRI is necessary here. For a coil array with  $N$  coils, the signal in the  $j^{\text{th}}$  coil is given by [10, p. 25]:

$$s_j(t) = \int \rho(\mathbf{x}) c_j(\mathbf{x}) e^{-2\pi i \mathbf{k}(t) \mathbf{x}} d\mathbf{x} + n(t)$$

with the proton density  $\rho$ , the complex-valued spatial sensitivity profiles  $c_j$ , receiver noise  $n$ , and the used time-dependent  $k$ -space trajectory  $\mathbf{k}(t)$ . For MRI reconstruction, this has to be discretized and becomes ([10, p. 32])

$$\mathbf{s} = P_k \mathcal{F} C \boldsymbol{\rho} + \mathbf{n} \quad (2.1)$$

where  $C$  is the multiplication with the spatial sensitivity profiles (coil profiles),  $\mathcal{F}$  is the discrete Fourier transform, and  $P_k$  is the projection onto the trajectory.

If the spatial sensitivity profiles (or coil profiles) are known, this can be regarded as a linear inverse problem ([10, Ch. 3.4.2])

$$\mathbf{y} = A \mathbf{x} + \mathbf{n}$$

with  $A = P_k \mathcal{F} C$ . The parallel imaging techniques mentioned in Section 2.1.1 can be understood as two-step approaches, first estimating the coil profiles from calibration data and then solving this linear inverse problem.

A problem with the two-step approach is that it does not use the available data optimally. The idea of NLINV is to jointly estimate image content and coil profiles, enabling better use of the available data and leading to higher image quality. Here, MRI is understood as a non-linear operator equation

$$F(\mathbf{x}) = \mathbf{y}, \quad \text{with } \mathbf{x} = \begin{pmatrix} \rho \\ c_1 \\ \vdots \\ c_N \end{pmatrix} \quad (2.2)$$

with an operator  $F$  that maps the unknowns, the proton density  $\rho$  and the coil profile  $c_i$  for each of  $N$  coils, to the measured  $k$ -space data  $\mathbf{y}$ .

For large undersampling factors both the linear and the non-linear parallel imaging problems become ill-conditioned, leading to noise amplification. Therefore, regularization is introduced to curtail the noise amplification.

In this thesis, the iteratively regularized Gauss-Newton method (IRGNM) is used to solve the non-linear problem. The operator  $F$  takes the following form (compare

Equation (2.1)):

$$F: x \mapsto \begin{pmatrix} P_k \mathcal{F} c_1 \rho \\ \vdots \\ P_k \mathcal{F} c_N \rho \end{pmatrix} \quad (2.3)$$

An obvious problem is the insufficient separation between  $c_i$  and  $\rho$ : multiplying each  $c_i$  by any complex function and dividing  $\rho$  by the same function leaves the product unchanged. Even the extreme case of all proton density information in the coil profiles  $c'_i = c_i \rho$ ,  $\rho' \equiv 1$  is possible without further constraints. Since coil profiles are generally smooth, this problem can be solved with a regularization term penalizing high  $k$ -space frequencies in the coil profiles.

As further regularization, the distance to an initial guess can be used. In the context of real-time MRI, a slightly different approach is useful: As long as the frame rate is sufficiently high to resolve the dynamics of the measured object, subsequent frames will be very similar. So instead of a penalty on the difference to an initial guess, the difference to the preceding frame is penalized, constituting a form of temporal regularization.

Constraining the reconstruction through prior knowledge in this way is necessary to recover the data missing because of undersampling. A more detailed description of the IRGNM and its application to MRI can be found in Chapter 5 of Uecker [10] and in Uecker et al. [15]. The implementation of NLINV used in this thesis is described in Section 3.1.2.

## 2.3. Undersampling and Image Artifacts

Undersampled MRI acquisitions are the basis of the real-time MRI used in this thesis, because of the possibility for tremendous speedup. To understand undersampling, sufficient sampling must be introduced first. For radial sampling this leads to the following statement: For a quadratic field of view of length  $L$  and a desired resolution  $\Delta x$  determined by the highest sampled frequency  $k_{\max} = \frac{1}{2\Delta x}$  in  $k$ -space, the Nyquist criterion states that the angular spacing  $\Delta\phi$  between the spokes has to fulfill [7, p. 906]

$$k_{\max} \Delta\phi \leq \frac{1}{L}.$$

Or equivalently the number of spokes  $n_{\text{spokes}}$  has to fulfill

$$n_{\text{spokes}} \geq \pi L k_{\max} \quad (2.4)$$

Compared to the needed number of phase-encoding steps  $n_{\text{phase}}$  in Cartesian sampling

$$n_{\text{spokes}} = \frac{\pi}{2} n_{\text{phase}} \quad (2.5)$$

holds, so approximately 57 % more excitations are necessary [7, p. 906].

For real-time MRI, full Nyquist sampling per frame is too slow, so far fewer spokes are generally recorded. The effects that this undersampling has on images can be understood using the point spread function (PSF). It is the image of a single point produced by the imaging process under consideration. So the image of an extended object is the convolution of this object with the PSF. In MRI, the PSF is determined by the  $k$ -space sampling pattern. Figure 2.3a shows the PSF for a fully sampled radial acquisition. The PSF consists of a central lobe determining the shape of an imaged point, surrounded by a region where it is close to zero (called the artifact-free region), in turn surrounded by artifact-generating side-lobes. In Figure 2.3a, the artifact-free region covers the entire FOV. Using only half the Nyquist-dictated number of spokes as in Figure 2.3b leads to larger side lobes covering the edge of the FOV, while even lower numbers of spokes almost completely eliminate the artifact-free region (Figures 2.3c and 2.3d).

The artifacts generated by this imperfect PSF are mostly streak artifacts, which are generated by each pixel of the object at a distance determined by the extent of the artifact-free region. For real-time MRI, it is common to record less than 20 spokes per frame, leading to a large problem with streak artifacts (Figure 2.3d). Since the image is the convolution of the PSF with the object, high intensity regions of the object will generally lead to more intense streak artifacts.

The problem of artifacts is partly mitigated by NLINV, through temporal regularization: the PSF and therefore the streak artifacts are different in subsequent frames, so temporal regularization leads to a dampening. But since streak artifacts are still a significant problem in some real-time MRI acquisitions, another possible mitigation strategy based on coil selection is the subject of Chapter 5.

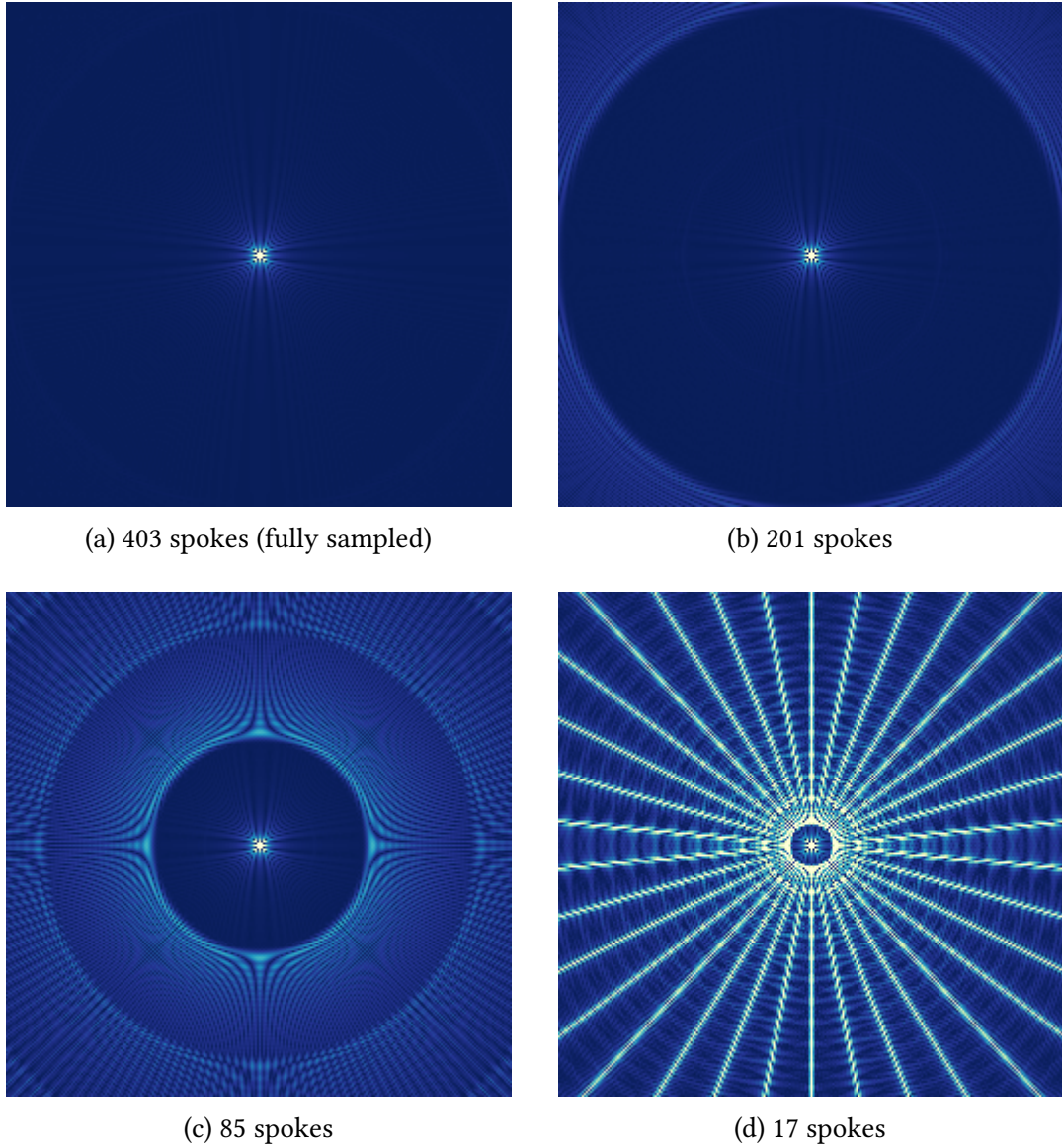


Figure 2.3: Absolute value of simulated point spread functions for (a) 403, (b) 201, (c) 85, and (d) 17 spokes. The FOV size is  $256 \times 256$ . According to Equation (2.5), full Nyquist sampling requires more than 402 spokes. 17 and 85 spokes were chosen since those are common values for the number of spokes per single frame and per full frame in real-time MRI (for a definition of the terminology see Section 3.1).

## 3. Methods

### 3.1. Data Acquisition and Processing

All data used in this thesis was acquired using a MAGNETOM Prisma<sup>fit</sup> system (Siemens Healthcare, Erlangen, Germany) at a field strength of 3 T. For cardiac and abdominal measurements a 32-channel coil array was used, consisting of anterior and posterior 16-channel arrays. For head measurements a 64-channel head coil was used. Phantoms used either coil array.

A radial FLASH sequence developed in the insitute was used for acquisition. This sequence uses a turn-based pattern, where a set of  $n_{\text{spokes}}$  spokes is acquired for each frame. For the subsequent frame, this pattern is rotated by  $2\pi/n_{\text{turns}} \cdot n_{\text{spokes}}$ , so that after  $n_{\text{turns}}$  frames the patterns overlap again. This is illustrated in Figure 3.1.  $n_{\text{turns}}$  frames taken together, containing all spoke orientations, are called a *full frame*.

Acquisition parameters for the datasets used in this thesis can be found in Table B.2 in Appendix B, while descriptions of the datasets are gathered in Table B.1. Dataset labels are typeset in small capitals (e.g. HEAD1) so that they can be quickly identified.

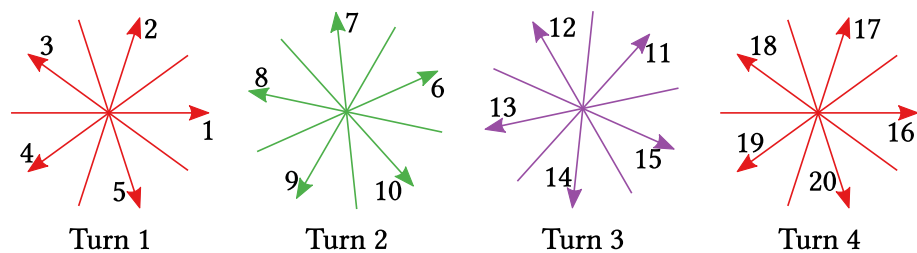


Figure 3.1: Diagram showing an acquisition with 5 spokes and 3 turns. The numbers next to the spokes show the order in which they are acquired. Between spokes, there is an angle of  $360^\circ/n_{\text{spokes}}$  (here:  $360^\circ/5 = 72^\circ$ ), between turns an angle of  $360^\circ/n_{\text{spokes}} \cdot n_{\text{turns}}$  (here:  $360^\circ/5 \cdot 3 = 24^\circ$ ). The  $(n_{\text{turns}}+1)^{\text{th}}$  turn is again identical to the first turn.

#### 3.1.1. Pre- and Postprocessing

There are several pre- and postprocessing steps applied to the measured data. First is a gradient delay correction using the first full frame: due to imperfect gradient timing in the MRI system, the actually measured  $k$ -space trajectory deviates from the expected trajectory. This can partly be corrected by gradient delay correction. The procedure is described in detail in Chapter 4 of Untenberger [16]. Then, the data is compressed by a principal component analysis (PCA) to fewer channels. This procedure is described in Chapter 4. The corrected and compressed data is then interpolated on a square Cartesian grid in a procedure called *gridding*, described, for example, in Chapter 13.2 of Bernstein, King, and Zhou [7]. For better accuracy of the interpolation, the Cartesian grid is chosen with a 1.5 times higher sample density than the originally sampled  $k$ -space data. This is called *overgridding*. The gridded frames are then reconstructed using NLINV.

The postprocessing steps depend on the application. For anatomical real-time MRI, a pixelwise temporal median filter is applied: Each pixel in frame  $n$  is replaced by the median of the same pixel in the frames  $n \pm \lfloor \frac{n_{\text{turns}}}{2} \rfloor$ . A non-local means filter for image denoising, described in Klosowski and Frahm [17], is applied next.

For other applications, different postprocessing steps are needed. For phase-contrast flow imaging the phase difference map needs to be calculated, for example.

All pre- and postprocessing steps are available in two implementations: a MATLAB<sup>1</sup> implementation and integrated in `nlinv++`. The MATLAB implementation is used for testing and implementing new techniques, while `nlinv++` can be used directly on the MRI scanner.

#### 3.1.2. `nlinv++`

`nlinv++` is a C++ program written in the institute. It can be used online (i.e. on the MRI scanner) and offline. The online version is running as a “bypass server”, so instead of forwarding the data to the vendor-supplied reconstruction pipeline, it is send to the custom reconstruction pipeline instead. The reconstructed images are then written back to the scanner, yielding seamless integration. Offline, `nlinv++` can be used to reconstruct previously measured data again.

`nlinv++` is itself implemented as a pipeline. It consists of five pipeline stages, each running in its own thread with an additional thread for the controlling stage. The five pipeline stages are: `datasource`, `preprocessor`, `reconstructor`, `postprocessor`, and `data-sink`. The stages are connected by channels, which are implemented as thread-safe

---

<sup>1</sup>MATLAB is a registered trademark of The MathWorks, Massachusetts, USA.

type-erased lists, so any kind of message may be passed along the pipeline. Each pipeline stage decides on the appropriate action based on the type of this message<sup>2</sup>. Since the NLINV algorithm contains Fourier transforms and matrix-products of large matrices, the reconstructor stage uses graphics processing units (GPUs) to accelerate computation.

`nlinv++` is running on dedicated Supermicro SuperServer 4027GR-TR system with the Ubuntu 14.04 operating system, 2x Intel Xeon Ivy Bridge E5-2650 main processors, 8x NVIDIA GTX Titan Black (Kepler GK110) GPUs as accelerators, and 128 GiB main memory.

The setup is as follows: the controlling main thread starts up and sets up the configuration. It then starts up each of the pipeline stages:

**datasource** It reads in the raw measured data, either from a file or from a pipe connected to the scanner. It buffers data until enough data for one frame has been read and then sends it on.

**preprocessor** It receives the raw data from the datasource one frame at a time. It uses the first full frame as calibration data to calculate the gradient delay values and the coil compression matrix. It applies gradient delay correction, coil compression and gridding to each frame. Coil compression is discussed in more detail in Chapter 4.

**reconstructor** The reconstructor is the only stage that is itself multithreaded, commonly using up to 4 threads. Each thread is identical, and each reads its input from the common channel coming from the preprocessor. Since 8 GPUs are available, each of  $n_{\text{threads}}$  reconstructor threads distributes its data onto  $\lfloor \frac{8}{n_{\text{threads}}} \rfloor$  GPUs. Each thread independently reconstructs its frame and places it in the channel to the postprocessor.

**postprocessor** Receives reconstructed frames from the reconstructor and applies appropriate postprocessing to them. In most cases, that means temporal median and non-local means filtering. For phase-contrast flow MRI for example, it includes calculation of the phase-contrast map.

**datasink** Receives postprocessed images and writes them to file. Since the reconstructor is multithreaded, it might receive frames out-of-order. In that case, it buffers the out of order frames while waiting for the next in-order frame.

---

<sup>2</sup>The type is only erased inside the channels, it is recovered in the pipeline stages to decide on the action to be taken.

Once all data has been read, the datasource produces a finished message. Each subsequent pipeline stage that receives this message produces its own finished message and exits as well. The datasink, after having written all output data, produces a finished message for the controlling main thread. This final message acts as a control that the reconstruction finished successfully.

## 3.2. Data Visualization

The 2D images in this thesis are created using `arrayShow`<sup>3</sup>. Unless otherwise indicated, images are individually windowed. This ensures that comparisons between images are not unduly influenced by, for example, differences in total signal content. Furthermore, since the data analyzed in this thesis stems from real-time MRI acquisitions, they are properly understood as movies rather than still images. Therefore, representative individual frames were selected for this thesis.

Figure 3.2 shows the colormaps used in this thesis. For ease of identification, the colormap in Figure 3.2a is used to directly represent complex data, while the colormap in Figure 3.2b is used when showing the magnitude of complex data. A plain grayscale colormap is used for purely real data.

The comparison of different methods in this thesis is done by visual inspection of images, or by inspecting their difference. This is done since no generally accepted criterion for quantification of image quality exists in MRI, and since medical images are traditionally interpreted through visual inspection by physicians. Furthermore, the postprocessing filters described in Section 3.1.1 are not used on the images, so that the comparison is not unduly influenced by them.

---

<sup>3</sup><https://github.com/BiomedNMR/arrShow>, `arrayShow` is a MATLAB image viewer for multidimensional arrays, with a focus on MRI images.



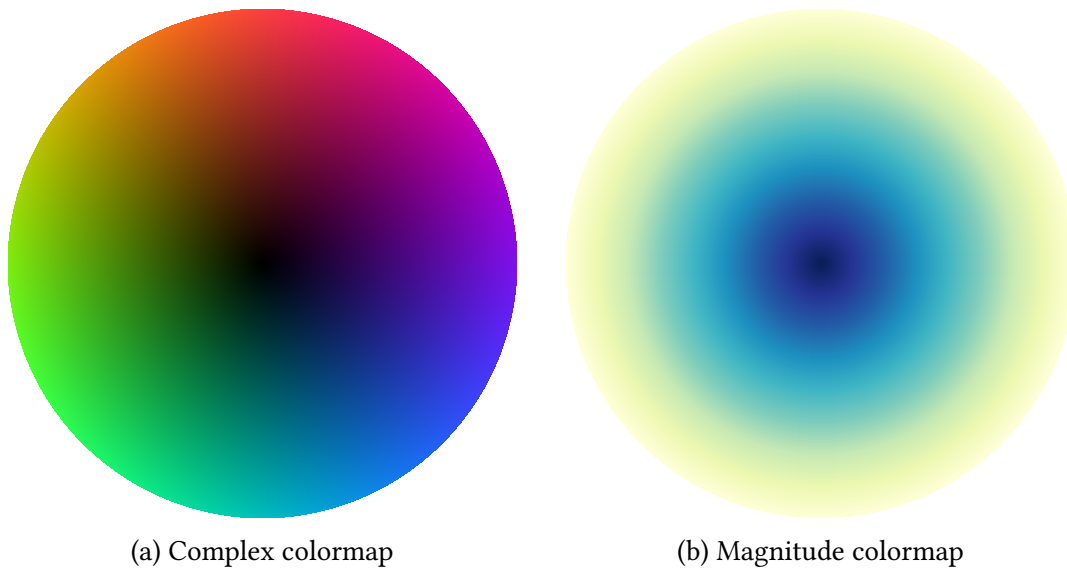


Figure 3.2: Colormaps used in this thesis. Both (a) and (b) show the complex unit disk. (a) shows the colormap used for directly representing complex-valued data, with hue indicating phase angle and brightness indicating absolute value. (b) shows the colormap used for representing the magnitude of complex data. The colormap in (a) is the standard colormap of `arrayShow` for complex data, while the colormap in (b) is the `YlGnBu_r` (“yellow, green, blue, reversed”) colormap from the `matplotlib` project, optionally available in `arrayShow`. Purely real data is visualized with a grayscale colormap.



## 4. Coil Compression

A challenge in modern MRI is the large amount of measurement data that can be acquired with current systems. Arrays of 32 or 64 coils are in routine use today, with even larger numbers of coils in consideration[18]. The use of very fast imaging techniques in real-time MRI exacerbates this problem. One advantage of multiple receiver coils is the possibility of parallel imaging for improved image quality and faster acquisition. The drawback is increased computation time.

A way to address this problem is coil compression, that means finding a smaller approximation of the data that still captures as much of the contained information as possible. One possibility is combining the measured coils into a smaller set of “virtual coils”, which is the approach taken here. One very fast approach is the use of linear combinations of coils, calculated from some initial calibration data. This enables the use of the once calculated compression operator on new data as it is coming in, in a way suitable for online use. Furthermore, the channel compression can be represented as a matrix product with the incoming data, which is advantageous because of the wide availability of highly optimized matrix-matrix-product routines.

Especially the ease of online use is the reason why a linear method was chosen for the current `nlinv++` implementation, namely PCA.

### 4.1. Principal Component Analysis

Principal component analysis (see [19] for a general introduction) is a technique for dimensionality reduction and feature extraction used in statistics. Here, the dimensionality reduction is the important characteristic.

#### 4.1.1. The PCA Algorithm

The input of the PCA algorithm is the ungridded raw data of the first full frame from scanner. This data consists of the measured samples for each line for each coil, so it is an array of dimensions  $n_{\text{coils}} \times n_S \times n_{\text{samples}}$ , which for PCA is treated as a matrix of

#### 4. Coil Compression

dimensions  $n_{\text{coils}} \times n_S \cdot n_{\text{samples}}$ . Here,  $n_S = n_{\text{spokes}} \cdot n_{\text{turns}}$  is the number of spokes in a full frame.

1. Take the input matrix  $A$  of size  $n_{\text{coils}} \times n_S \cdot n_{\text{samples}}$  and calculate the  $n_{\text{coils}} \times n_{\text{coils}}$  matrix  $\text{cov}(A) := A^* \cdot A$ , where  $*$  is the conjugate transpose operation.  $\text{cov}(A)$  is related to the covariance matrix of  $A$ , but differs in two important aspects. First, the covariance matrix requires the columns of  $A$  to have zero mean. This is not guaranteed for MRI data. The column means are, however, close enough to zero to have negligible influence on the method. Second, the covariance matrix needs to be scaled by  $1/n_{\text{samples}}$ , which  $\text{cov}(A)$  is not.<sup>1</sup>
2. Find an eigenvalue decomposition of  $\text{cov}(A)$ , that means a unitary transformation matrix  $I$  and a diagonal matrix  $\Lambda$  so that  $\text{cov}(A) = I^* \cdot \Lambda \cdot I$ .  $\Lambda$  contains the eigenvalues of  $\text{cov}(A)$  on its diagonal, and all eigenvalues are real since  $\text{cov}(A)$  is a normal matrix<sup>2</sup>.
3. Jointly permute  $I$  and  $\Lambda$  so that the eigenvalues on the diagonal of  $\Lambda$  are in descending order.
4. Use the first  $n_{\text{pc}}$  columns of  $I$  as the compression matrix, where  $n_{\text{pc}}$  is the desired number of principal components.

This method can be understood in the following way: By applying  $I$  to the input data it is transformed into a different coordinate system. In this system, the diagonal entries of  $\Lambda$  are a measure of the variation contained in each direction. The variation contained in the  $i^{\text{th}}$  direction can be calculated as  $\Lambda_{ii}/\text{tr}(\Lambda)$ , where  $\text{tr}()$  is the trace. So the first  $n_{\text{pc}}$  columns of  $I$  are a transformation matrix which retains  $\sum_{i=0}^{n_{\text{pc}}} \Lambda_{ii}/\text{tr}(\Lambda)$  of the variation in  $A$ . This normalization with  $\text{tr}(\Lambda)$  is the reason why it is enough for the eigenvalues of  $\Lambda$  to be proportional to the covariances.

##### 4.1.2. Application in real-time MRI

For real-time MRI, the PCA algorithm is applied as a preprocessing step. In the preprocessor stage (see Section 3.1.2 for a discussion of the pipeline stages), the data of the first full frame is used as input for the algorithm. In the current implementation,  $n_{\text{pc}} = 10$ , that is the first 10 principal components are used. This is a heuristically obtained, conservative

---

<sup>1</sup>So  $\text{cov}(A)$  can only be proportional to the covariance matrix. However, this is sufficient, as will be explained later.

<sup>2</sup>A matrix  $M$  is normal if  $M \cdot M^* = M^* \cdot M$ , which is obviously fulfilled for  $\text{cov}(A)$

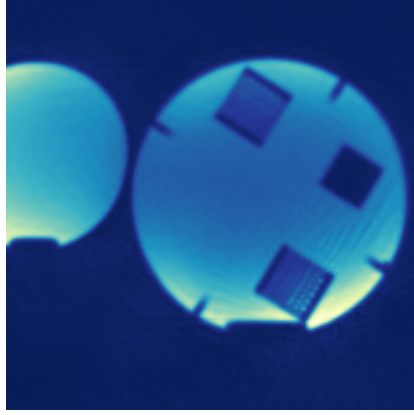
value [20, Ch. 6.3]. Images for comparison between  $n_{\text{pc}} = 10$  and  $n_{\text{pc}} = n_{\text{coils}}$  are shown in Figure 4.1.

There are several shortcomings of this approach:

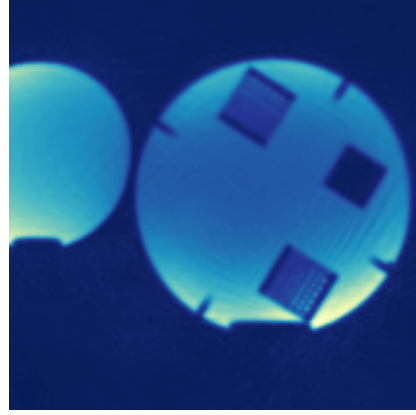
1. It is independent of the image under consideration. Some images, especially of phantoms, can naturally be described by fewer components. Furthermore, the number of imaging coils is not taken into consideration. Using 10 principal components will have vastly different results when using e.g. a 12-channel compared to a 64-channel head coil.
2. 10 only has 2 and 5 as factors. When distributing coil data onto accelerators for reconstruction (as described in Section 3.1.2), this might lead to some accelerators containing more coil data to calculate than others. This will slow down the accelerators having to do more work, and through synchronization between the accelerators slow down the whole reconstruction.
3. PCA finds “virtual coils” (directions) of highest variance. But this is not necessarily optimal for MRI: PCA will favor areas of high signal intensity at the expense of areas of lower intensity, creating not only non-uniform image appearance, but it can also lead to higher noise levels, since the coils with high sensitivity in the regions of low intensity will be weighted less. This effect, of course, is less pronounced at higher numbers of principal components.

Therefore, an optimized coil compression algorithm was investigated in this thesis, in order to lower the number of necessary principal components and thereby improve reconstruction speeds.

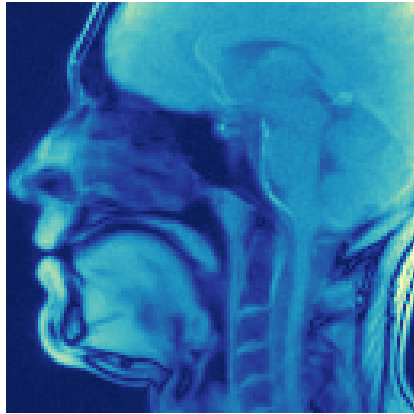
#### 4. Coil Compression



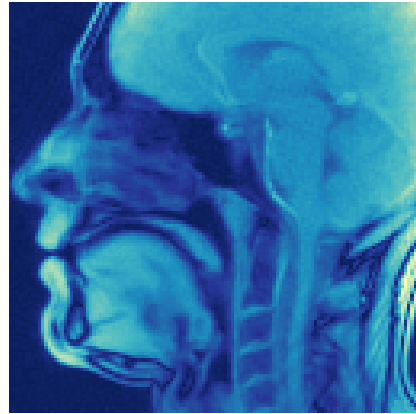
(a)  $n_{\text{pc}} = \text{full}$



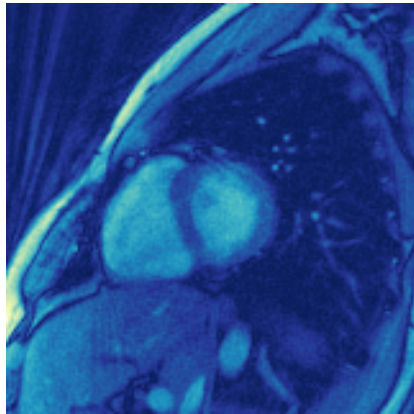
(b)  $n_{\text{pc}} = 10$



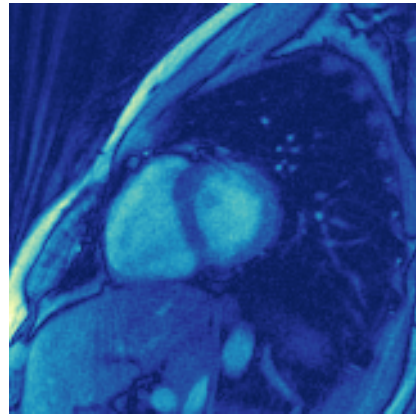
(c)  $n_{\text{pc}} = \text{full}$



(d)  $n_{\text{pc}} = 10$



(e)  $n_{\text{pc}} = \text{full}$



(f)  $n_{\text{pc}} = 10$

Figure 4.1: Comparison of using 10 principal components vs. using the full dataset for a water phantom (PHAN1) (a)–(b), a sagittal slice through a human head (HEAD1) (c)–(d), and a two-chamber view of a human heart (HEART1) (e)–(f). The difference in image quality is negligible. As an example Figure 4.2 shows the magnitude of the complex difference between (c) and (d).

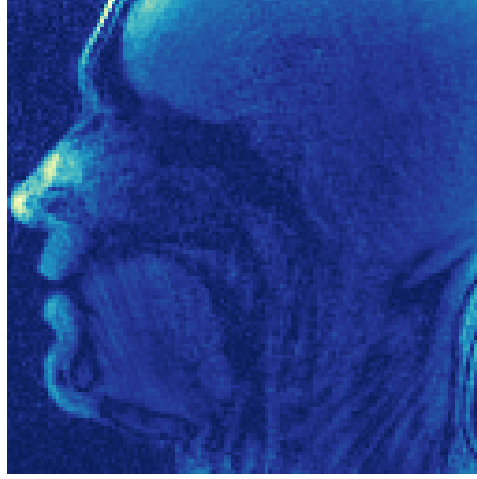


Figure 4.2: Magnitude of the complex difference between Figures 4.1c and 4.1d, shown as an example. Since the image is mostly noise with only little structure in the high intensity regions, it can be concluded that the PCA compression to 10 coils does not impact image quality too much.

## 4.2. Optimized Combination

In order to address these shortcomings of PCA for MRI, Buehrer et al. [21] have introduced an optimized coil compression algorithm for SENSE MRI [12]. A MATLAB implementation adapted for real-time MRI was already available in the institute<sup>3</sup>, and was used for evaluation of the method.

The optimized algorithm tries to overcome some of the shortcomings of plain PCA, especially the non-uniform image appearance and the possible noise enhancement by using the coil profiles as weighting. Figures 4.3 to 4.5 show the different steps of the algorithm applied to a water phantom dataset (PHAN1).

1. Input to the optimized algorithm are the  $n_{\text{pixels}} \times n_{\text{pixels}}$  proton density  $R$  (Figure 4.3a) and the  $n_{\text{pixels}} \times n_{\text{pixels}} \times n_{\text{coils}}$  coil sensitivity profiles  $C$  (Figure 4.4) of a finished NLINV run. Generate a  $n_{\text{pixels}} \times n_{\text{pixels}}$  weighting matrix  $W$  with  $\forall i,j W_{ij} = 1$ .
2. Only consider pixels of moderately high image intensity. The threshold for this was set at 5 % of the maximum intensity: Set  $W$  to zero at  $\{(i,j) \mid R_{ij} < \min(R) + 0.05 \cdot (\max(R) - \min(R))\}$  (Figure 4.3b).
3. Calculate the combined sensitivity matrix  $S$ :  $S_{ij} = \sqrt{\sum_{c=1}^{n_{\text{coils}}} \|C_{ijc}\|^2}$ .

<sup>3</sup>Written by Soeren Wolfers as part of an internship program. Because of the limited duration of the internship, no performance evaluation was done at that time.

#### 4. Coil Compression

4. Normalize coil sensitivity in each pixel, i.e. divide  $W$  at each point  $(i,j)$  by  $S_{ij}$  (Figure 4.3c).
5. Only considers pixels of moderately high combined coil sensitivity. Here, the same threshold of 5 % of the maximum was chosen: Set  $W$  to zero at  $\{(i,j) \mid S_{ij} < \min(S) + 0.05 \cdot (\max(S) - \min(S))\}$  (Figure 4.3d).
6. Calculate weighted coil sensitivities:  $C_{ijc}^w = C_{ijc} \cdot W_{ij}$  (Figure 4.5)
7. Transpose and interpret the  $n_{\text{pixels}} \times n_{\text{pixels}} \times n_{\text{coils}}$  weighted coil sensitivities matrix  $C^w$  as a  $n_{\text{coils}} \times n_{\text{pixels}}^2$  matrix and use the PCA algorithm described in Section 4.1.1.

This algorithm takes some insights into account. First, by using the proton density and coil sensitivity profiles, it is possible to exclude irrelevant pixels in the calculation. Furthermore, to generate more uniform image intensity and noise levels, the coil profiles are normalized prior to PCA compression. A disadvantage of this method is the need for the output of a finished NLINV run.



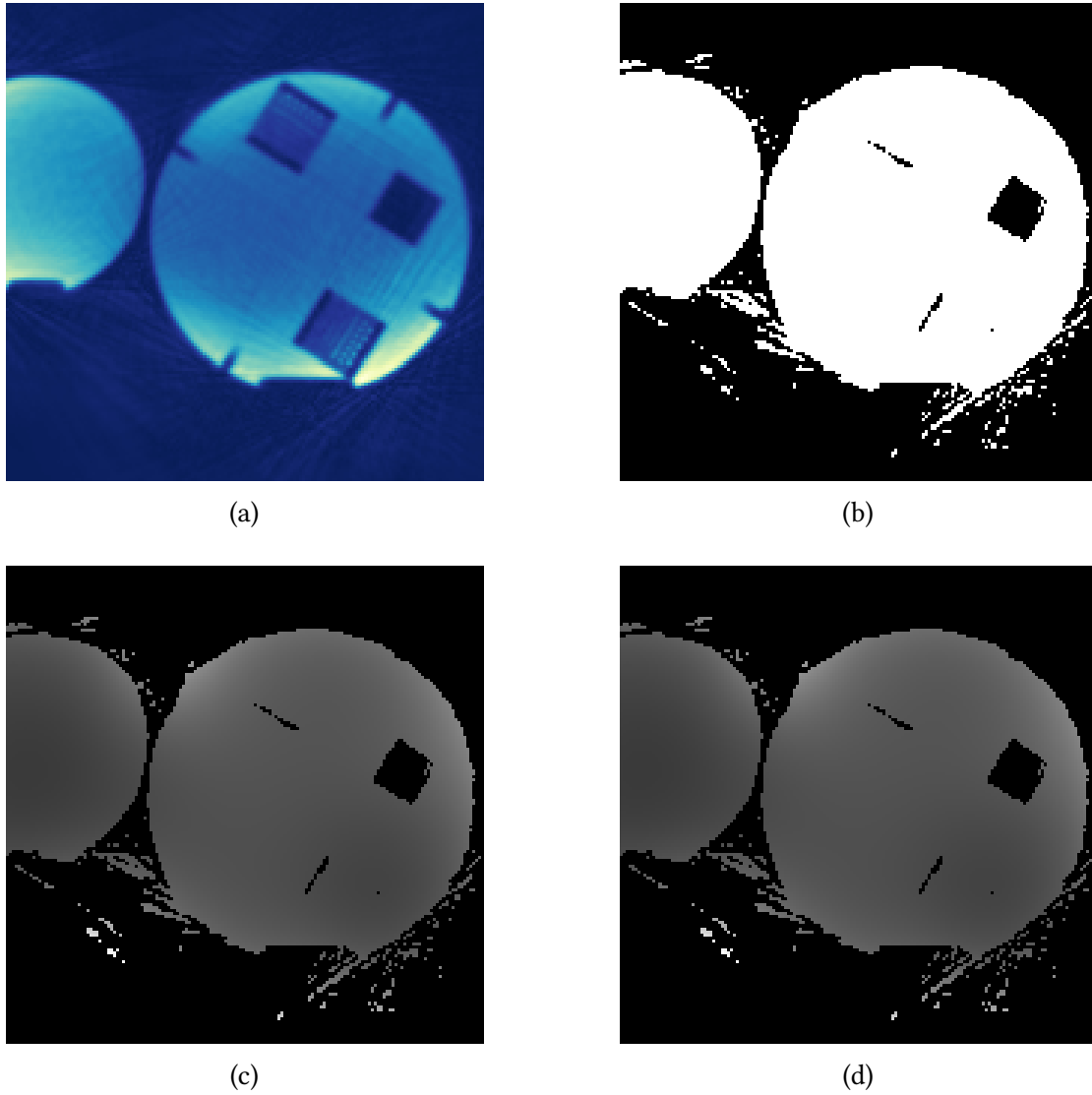


Figure 4.3: Visualization of different steps of the optimized algorithm. (a): magnitude of the input proton density  $R$ . (b)–(d): weighting matrix  $W$  after (b) 5 % thresholding of the proton density, (c) normalization with the combined sensitivities, (d) 5 % thresholding of the combined sensitivities. For this dataset this last step leaves  $W$  unchanged, since the combined sensitivities pass the threshold at every nonzero pixel.

#### 4. Coil Compression

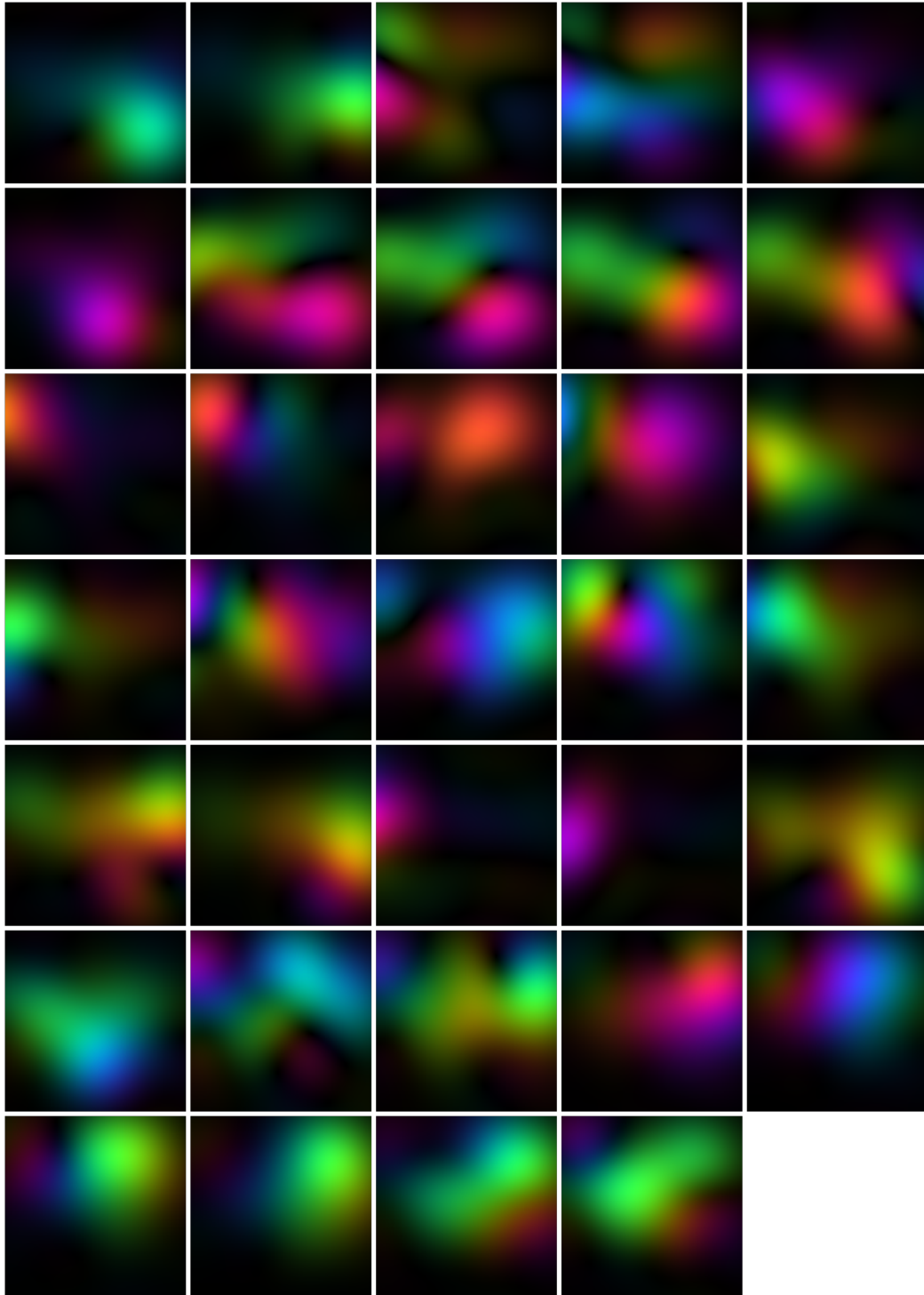


Figure 4.4: Complex-valued input coil profiles  $C$  for the optimized algorithm.

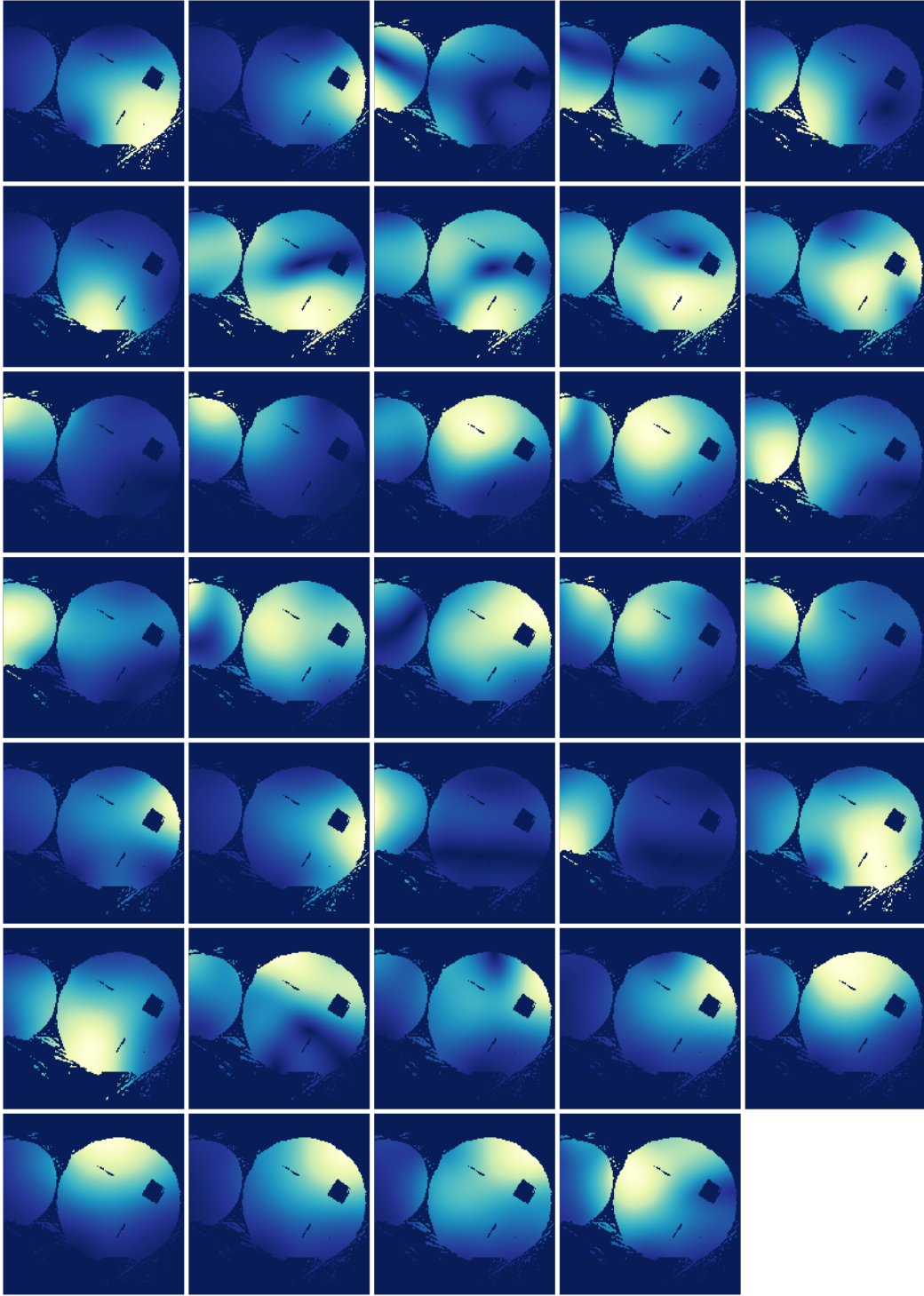


Figure 4.5: Weighted coil profiles  $C^w$  of the optimized algorithm, used as input for regular PCA.

### 4.3. Performance Evaluation

Since the optimized algorithm has not already been added into `nlinv++`, the performance evaluation was strictly done offline, using MATLAB. Routines implementing data reading and preprocessing (including gradient delay correction and gridding) were already available. For the reconstruction, a modified version of `nlinv++` was written as part of this thesis, which allows the input of data preprocessed in MATLAB and only uses the reconstructor and `datasink` stages described in Section 3.1.2. This was done to prevent subtleties in the reconstruction from influencing the results of the evaluation.

Figures 4.6 to 4.10 provide an overview of the improvement that can be expected from using the optimized compression algorithm over plain PCA.

As can be seen, for most datasets the improvement is limited to low numbers of principal components (2 and 4); for 8 and 10 components, the difference in all datasets is very small.

In the head datasets (Figures 4.6, 4.8 and 4.9) for 2 principal components, the improvement in image intensity uniformity can be clearly seen: The region of the lower jaw shows very low intensity in the PCA images and only acceptable intensity in the optimized images. This effect is less pronounced for higher numbers of principal components, where PCA has more uniform images also.

The optimized combination also reduces streak artifacts in some images, most notably between Figures 4.6d and 4.6e, and between Figures 4.9a and 4.9b. This can be understood as a consequence of image intensity uniformity: In PCA, coils with very high but localized intensity will be preferred. Streak artifacts originate from these high intensity regions in these images. By preferring uniform images, the relative intensity of the artifacts is reduced compared to the rest of the image.

For the water phantom (Figure 4.7) and the cardiac data set (Figure 4.10), the difference is small for all numbers of principal components.

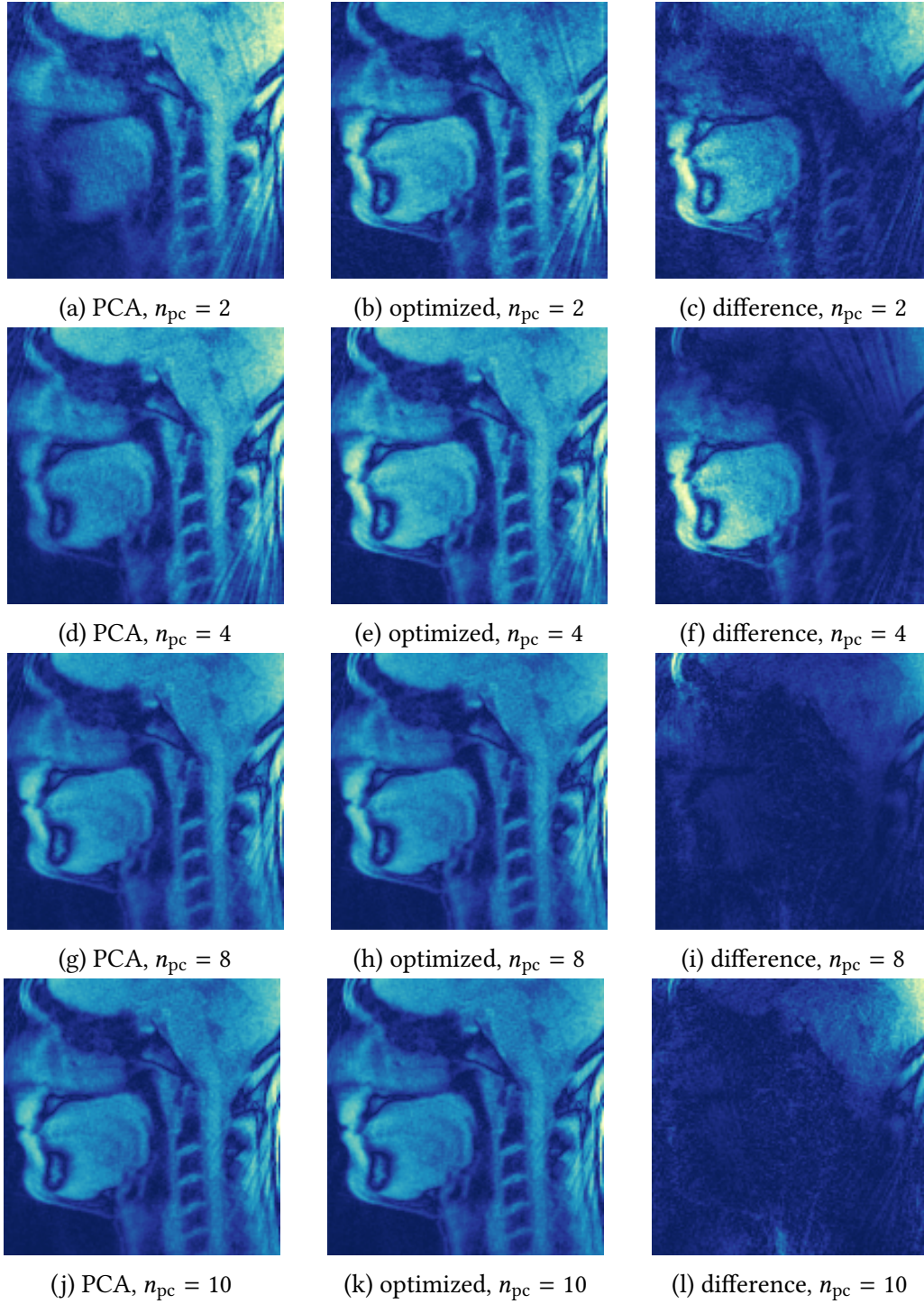


Figure 4.6: Dataset HEAD2 compressed with PCA (left column), the optimized combination (middle) and their difference (right column). For 2 and 4 principal components ((a)–(f)) the optimized combination yields clearly higher image quality, especially regarding intensity distribution: while (a) contains almost no intensity in the region of the lower jaw, (b) provides sufficient intensity there. For 8 and 10 principal components, there is almost no visual difference.



#### 4. Coil Compression

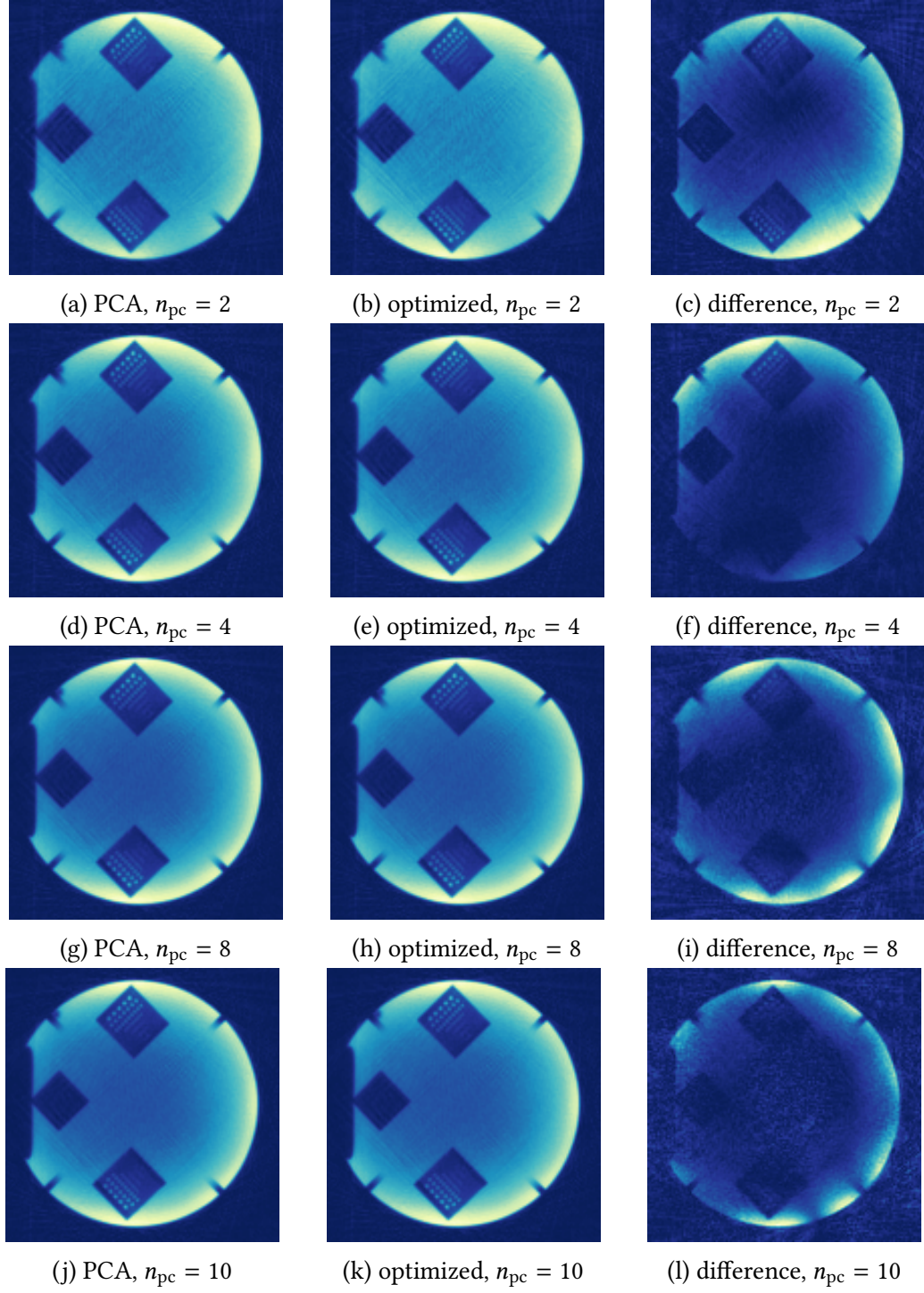


Figure 4.7: Dataset PHAN2 compressed with PCA (left column), the optimized combination (middle) and their difference (right column). While the SNR increases with increasing number of principal components, the visual difference between PCA and the optimized combination is negligible.

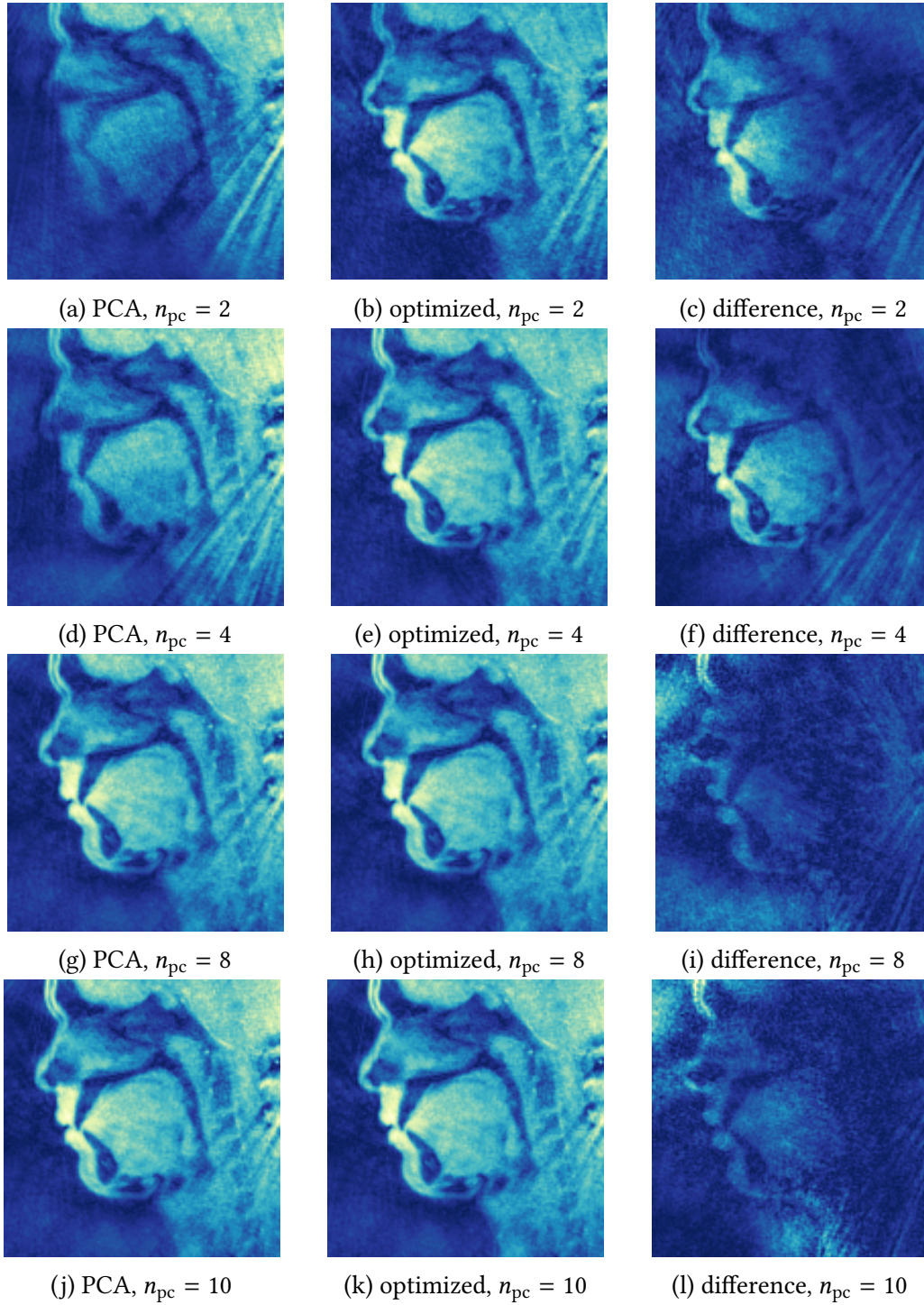


Figure 4.8: Dataset HEAD3 compressed with PCA (left column), the optimized combination (middle) and their difference (right column). For 2 and 4 principal components, the optimized combination yields preferable images, even reducing the severity of streak artifacts in the neck region between (d) and (e). For 8 and 10 principal components, the difference is negligible.



#### 4. Coil Compression

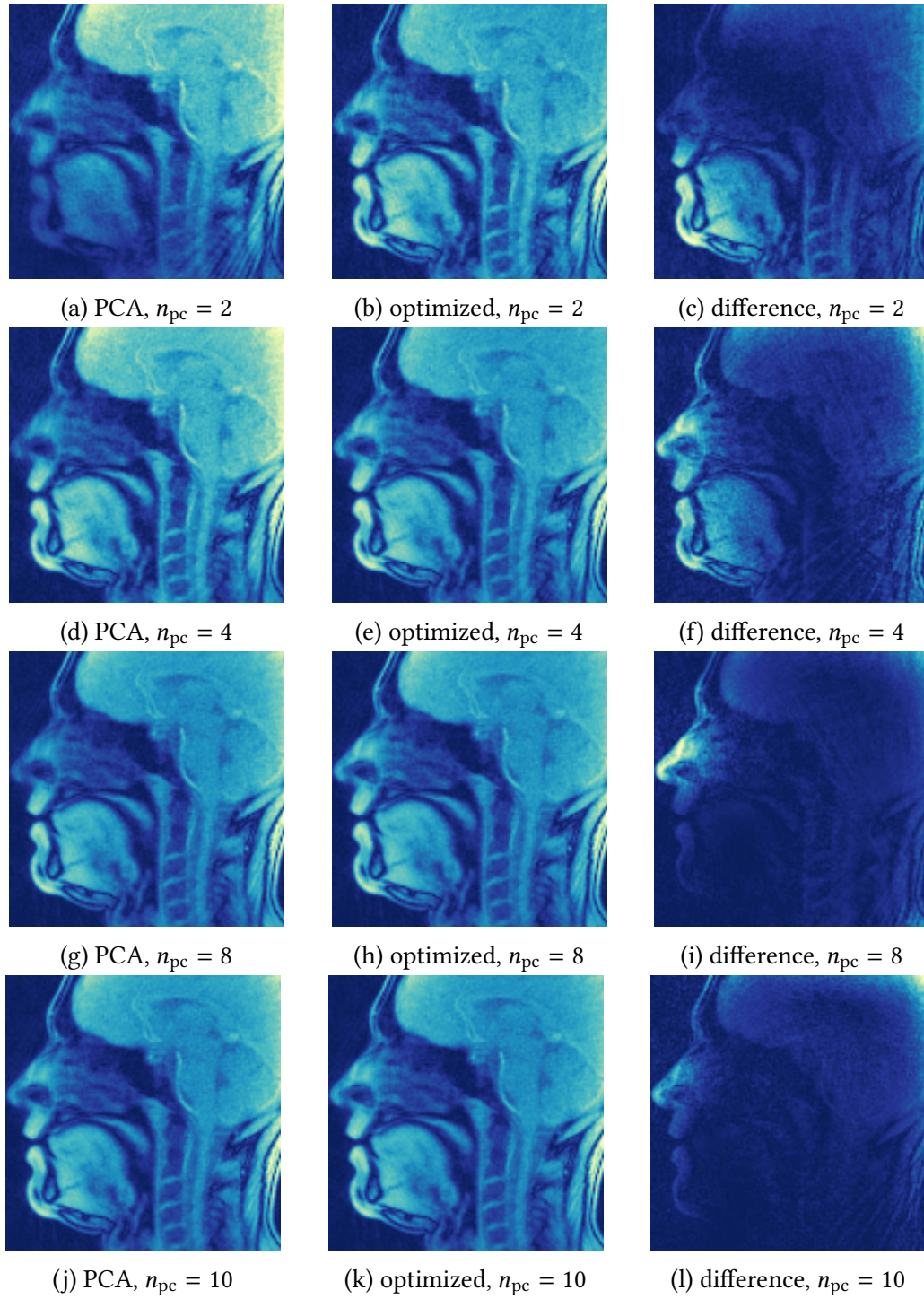


Figure 4.9: Dataset HEAD1 compressed with PCA (left column), the optimized combination (middle) and their difference (right column). For 2 principal components PCA suffers from reduced intensity in the region of the lower jaw and exhibits more severe streak artifacts in the neck region. For 4 principal components, PCA shows higher intensity at the right and top image border, but without major impact on image quality. For 8 and 10 principal components, the difference is negligible.



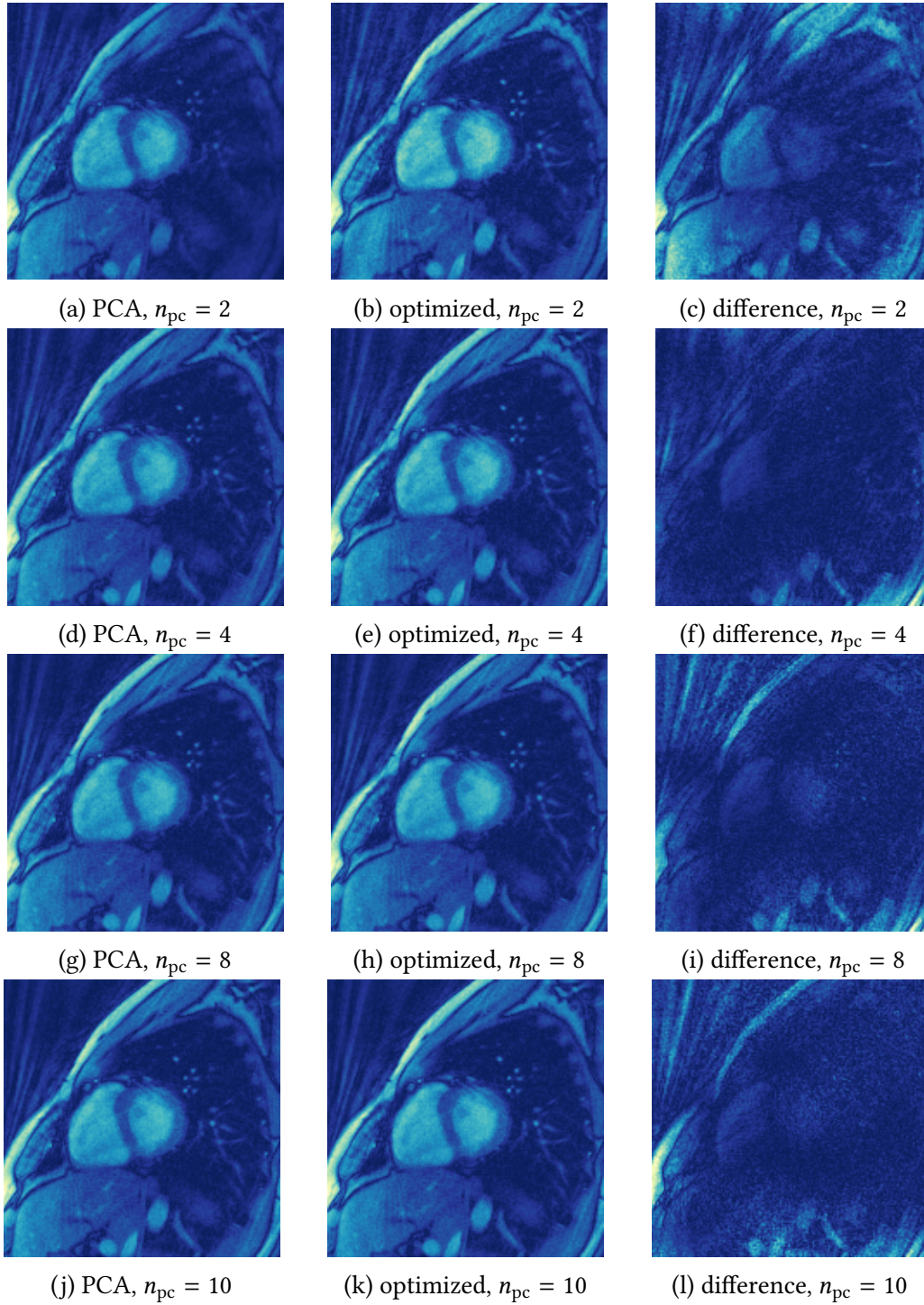


Figure 4.10: Dataset HEART1 (short-axis view of the human heart) compressed with PCA (left column), the optimized combination (middle) and their difference (right column). For 2 principal components, the optimized combination has slightly higher signal in the region around the heart. For 4, 8, and 10 principal components, the difference is negligible.

### 4.4. Discussion

Comparing the optimized combination to the current PCA method shows only improvement for 2 or 4 principal components. The same is true for the possibility of reducing the severity of streak artifacts.

The current implementation of the optimized combination requires the proton density and coil profiles from a finished NLINV. This is a problem in real-time MRI, where time is very constrained. It also runs against the current design of `nlinv++`, requiring feedback from the reconstructor to the preprocessor. This could conceivably be overcome by approximating the proton density and coil profiles: The proton density can be approximated as the root-sum-of-squares of all individually gridded coil data (which is the common method of combining multi-coil data, see Larsson et al. [11]), with the coil profiles approximated as the individual gridding reconstruction divided by the root-sum-of-squares image. But this only partly addresses the problem, gridding and reconstructing data from 64 coils or more can still take too much time to be feasible in real-time MRI.

In the end, reducing the number of principal components to 8 provides too little benefit to justify the switch to the optimized method, while reducing it to 4 or 6 principal components can lead to unacceptable SNR losses.

## 5. Coil Selection

Streak artifacts are a common problem in undersampled radial MRI [22–25]. Even for moderate undersampling image quality can be compromised. Though real-time MRI with NLINV does provide some mitigation (temporal regularization and median filtering, for example), it is still a problem in a large number of acquisitions. Figure 5.1 show examples of NLINV reconstructions with both median and non-local means postprocessing filters applied which still show streak artifacts.

The occurrence of streak artifacts can be understood as a confluence of several factors: As Section 2.3 showed, the degree of undersampling necessary for real-time imaging will invariably lead to artifacts in the resulting images. But most of these are unproblematic since the mitigation techniques in NLINV will greatly reduce the impact. Often, problems arise from objects outside of the FOV. Here, both the static magnetic field and the gradient fields show larger inhomogeneities, leading to overestimated and distorted signal intensity [26], which in turn leads to more intense streak artifacts. Streak artifacts are also often associated with fat which appears hyperintense in the  $T_1$ -weighted FLASH sequences used in real-time MRI, further amplifying the resulting artifacts.

The central insight justifying coil selection for streak artifact reduction is that only some coils contain data leading to streak artifacts in the reconstructed image: This can be seen by studying individual coil images. These can be reconstructed with plain gridding and subsequent Fourier-transform of individual coil data. Some examples of such individual coil images are shown in Figures 5.2 and 5.3, with prominent streak artifacts in only a subset of coils. Furthermore, excluding those coils during reconstruction can greatly reduce or even remove streak artifacts. This can be seen in Figure 5.4, which shows the comparison of the reconstruction of the dataset shown in Figure 5.2 with all coils (Figure 5.4a) and with one coil removed (Figure 5.4b). Coil selection has to be applied before coil compression: After coil compression, individual coils cannot be separated out anymore, having been intermixed into the set of virtual coils.

## 5. Coil Selection

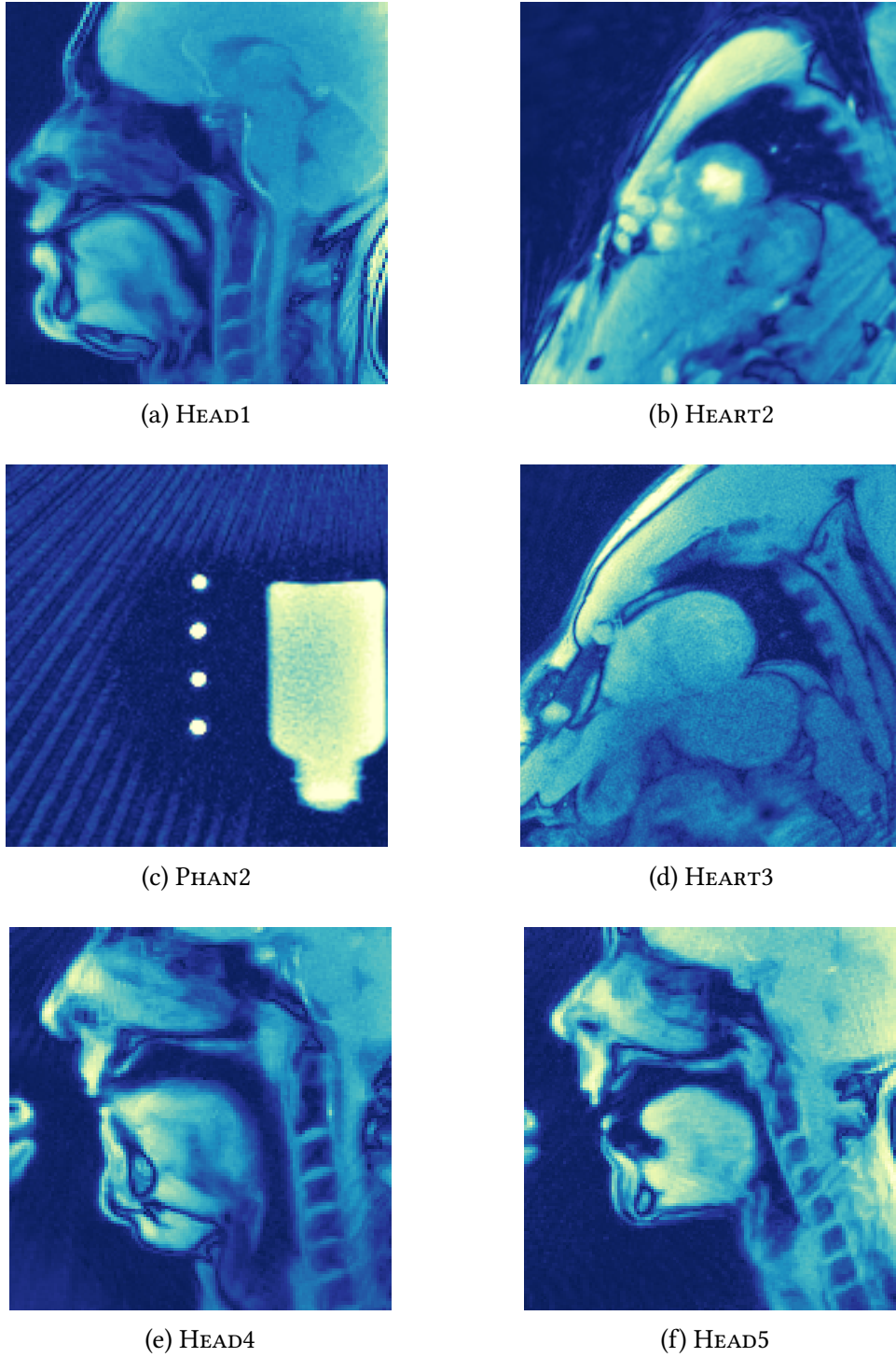
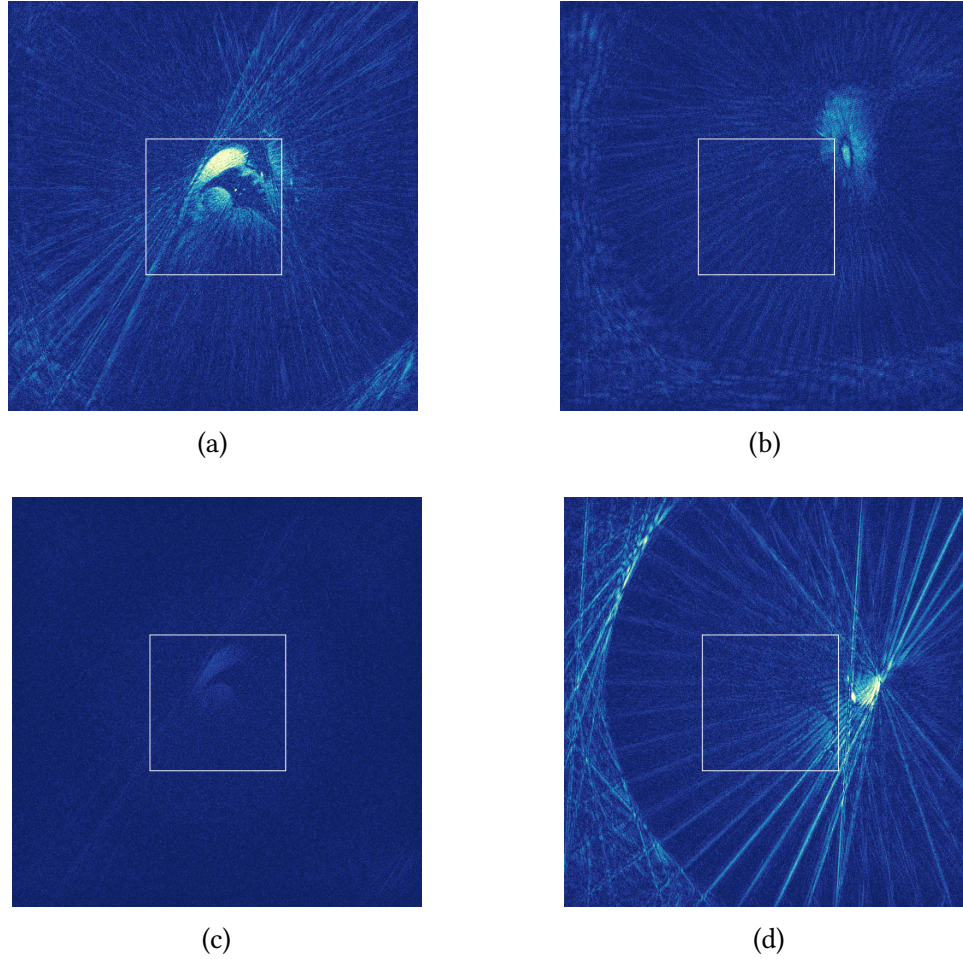


Figure 5.1: Examples of streak artifacts in real-time images. (a) streaks in the neck region, lower right, (b) streaks on the right side, (c) streaks coming from top, (d) streaks in lower right, (e) streaks in the neck region, lower right, (f) streaks in middle right (HEAD5). The streak artifacts are present even though the median and non-local means postprocessing filters were applied. In (c), the streaks originate from a counterflowing pipe outside of the FOV.





Figure 5.2: Gridding reconstructions of all 30 coils for HEART2. The white square indicates the selected FOV. The three times larger size of the image matrix is a consequence of 2 times oversampling and 1.5 times overgridding (see Section 3.1). Not all coils contribute useful signal inside the FOV: Some contain very little signal at all, while some only contain signal outside of the FOV. All images are shown with the same absolute windowing.





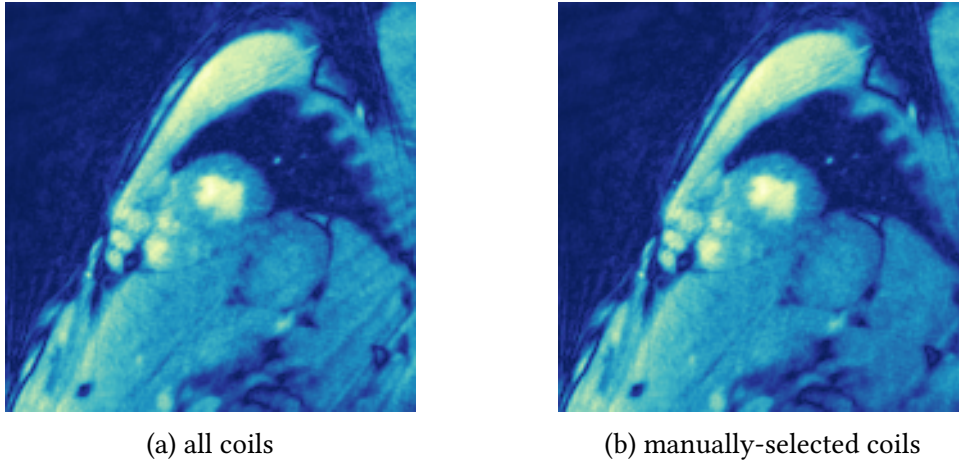


Figure 5.4: Comparison of NLINV reconstruction of HEART2 with (a) all coils and (b) without the coil shown in Figure 5.3d. As can be seen, the streaks in the middle right have been removed almost completely by excluding a single coil from the reconstruction.

## 5.1. Current Methods

### 5.1.1. Manual Selection

The most simple way of coil selection is manual selection, that means turning off unwanted coils before a measurement or ignoring some coils during reconstruction. For almost all MRI acquisitions, some coils are turned off: For example for a head measurement, spine coils integrated in the patient table are generally turned off. However, this is not feasible for routine use, since it is in general not possible to know which coils will produce artifacts.

### 5.1.2. Xue et al.

In [27], Xue et al. introduced a method which seeks to provide automatic coil selection. It is based on the insight that streak artifacts in radial imaging are associated with outer  $k$ -space: Low resolution images will typically not contain excessive streak artifacts. This can be immediately understood as a consequence of sampling: Close to the  $k$ -space center, there is inherently closer sampling in radial acquisitions: For a fixed number of spokes, the violation of the Nyquist criterion is stronger further out in  $k$ -space. The algorithm is:

1. Grid and reconstruct the magnitude images  $I_{\text{orig}}$  for all coils.
2. Apply a low-pass Hanning filter to the  $k$ -space data and reconstruct low resolution

## 5. Coil Selection

magnitude images  $I_{\text{ref}}$ .

3. Calculate the streak ratio  $R_{\text{streak}}$  given by  $R_{\text{streak}} = \frac{\text{mean}(|I_{\text{orig}} - I_{\text{ref}}|)}{\text{mean}(I_{\text{ref}})}$ .
4. Exclude coils where  $R_{\text{streak}}$  is larger than a predetermined threshold.

However, this approach is not fully automatic, it needs a predefined threshold for its streak ratio. This threshold needs to be manually found for the current application. Furthermore, it relies on image-space data, which means that data needs to be gridded and Fourier-transformed. Especially gridding is a very expensive operation, limiting the usefulness of this approach for real-time MRI. For these reasons, it was neither implemented nor evaluated in this thesis.

### 5.1.3. Grimm et al.

Grimm et al. [28] introduced an alternative coil selection method based on the algorithm of Xue et al. [27] which tries to overcome these deficiencies. It replaces the threshold above with a clustering method, thereby eliminating the need to manually set a threshold. Furthermore, it uses  $k$ -space data directly and does not need gridding.

The algorithm is:

1. Generate a high-pass filtered variant  $h_n$  and a low-pass filtered variant  $l_n$  of the ungridded  $k$ -space data for each coil  $n$ .
2. Calculate the streak ratio  $\tilde{R}_n$  by  $\tilde{R}_n = \frac{\|h_n\|_2}{\|l_n\|_2}$ .
3. Apply k-means clustering to separate the coils into two groups based on their  $\tilde{R}_n$ . Two values of  $\tilde{R}_n$  are randomly chosen as initial cluster centers.
4. Calculate the distance between the clustering centers. If it is less than twice the average standard deviation, repeat step 3 up to  $n_{\text{tries}}$  times. Otherwise, exclude the group of coils with high  $\tilde{R}_n$ .

Apart from the clustering and use of  $k$ -space data, it changes the Hamming window to a simple box window separating the data into high and low frequency parts, and changes the mean to the  $L^2$ -norm. Furthermore, the k-means algorithm can automatically find appropriate groups, while also providing a check to not exclude coils if no sufficiently separated groups can be found<sup>1</sup>. Furthermore, since it uses the ungridded raw data, it

---

<sup>1</sup>This is necessary since k-means will almost always generate two groups (if initialized with two centers), regardless of whether those groups exist in the data or not. Without such a basic check, the algorithm might exclude coils even if none of them contain any artifacts.



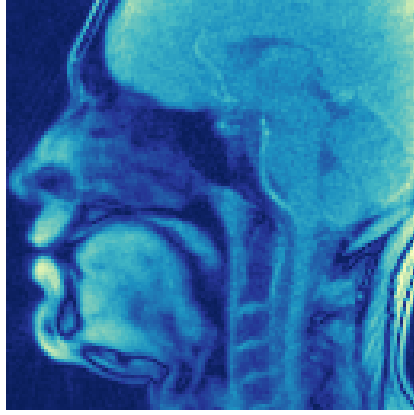
is very fast. The repetition of k-means<sup>2</sup> is done to ensure that the random choice of the initial cluster centers does not prevent k-means from excluding coils. The k-means algorithm itself and its random initialization make the algorithm non-deterministic: It is not guaranteed that consecutive runs will exclude the same coils. But for most datasets (and for all datasets shown in this thesis), the algorithm consistently gives the same results. Since no generally applicable value for the cutoff between high and low  $k$ -space was given, several cutoffs were tried. In the end, for an acquisition of  $n_{\text{samples}}$  samples, the inner  $n_{\text{samples}}/4$  were defined as the low  $k$ -space part  $l_n$ , with the rest assigned to  $h_n$ .

Figure 5.5 shows a comparison between using all coils and using Grimm et al.’s [28] selection for some datasets. As can be seen, Grimm et al.’s method [28] does not remove the prominent streak artifacts in a number of acquisitions. By examining the streak ratios  $\tilde{R}_n$  assigned to various coils (see Figure 5.6), it can be seen that often the values of  $\tilde{R}_n$  do not reflect the severity of the artifacts. Another problem is the algorithm’s behavior in the presence of mostly empty coils: Even if a coil does not contain usable signal, white receiver noise will still be present, possibly dominating the calculated streak ratios. This effect can be seen in Figure 5.7, for example. While excluding these coils does not negatively influence image quality, it also does not remove streak artifacts. In conclusion, the performance for this method for real-time MRI was not satisfactory.

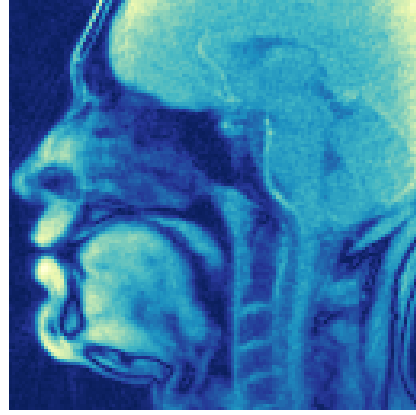
---

<sup>2</sup>Up to  $n_{\text{tries}} = 100$  times.

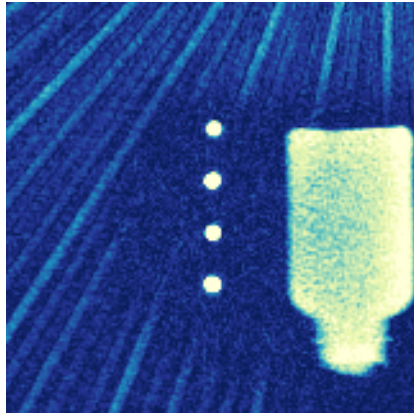
## 5. Coil Selection



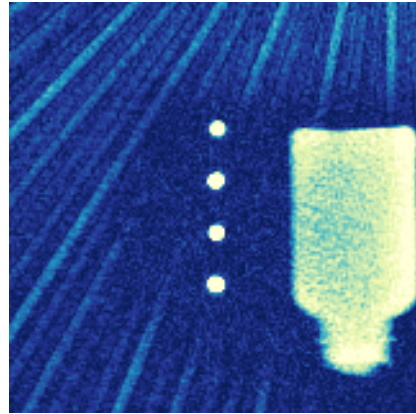
(a) HEAD1, all coils



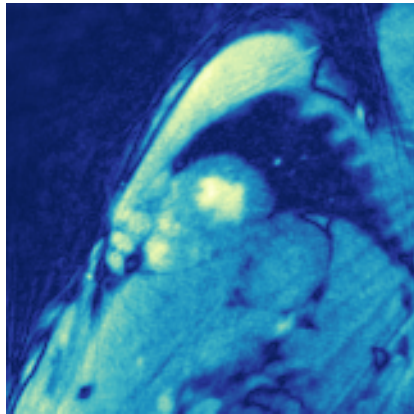
(b) HEAD1, Grimm et al. coils



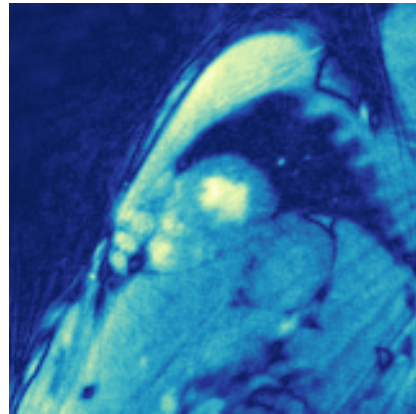
(c) PHAN2, all coils



(d) PHAN2, Grimm et al. coils



(e) HEART2, all coils



(f) HEART2, Grimm et al. coils

Figure 5.5: Comparison between using all coils (left column) and Grimm et al.'s [28] selection algorithm (right column) for several datasets. For HEAD1 ((a)–(b)), the streak artifacts in the neck region are removed almost completely, while the other datasets still contain significant artifacts. In all examples, coils were removed; the criterion described in step 4 did not apply.

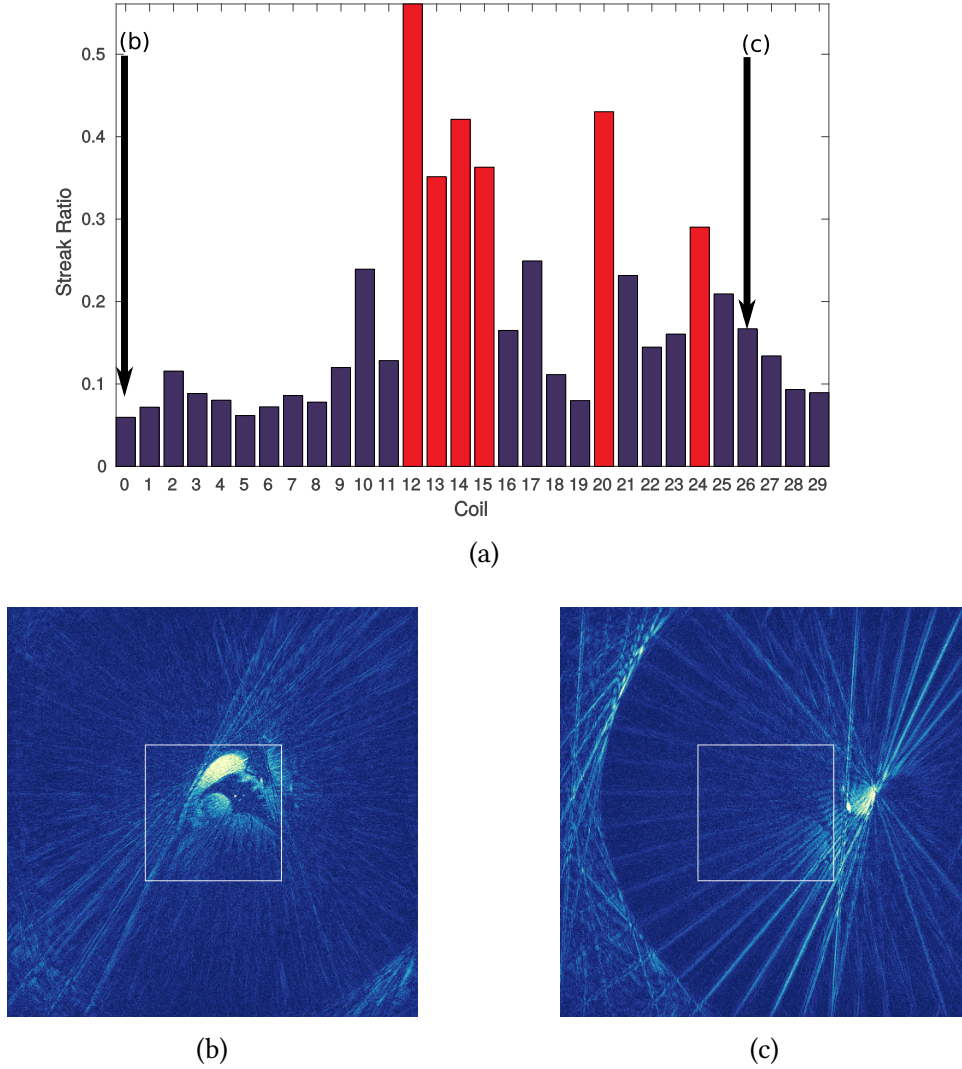
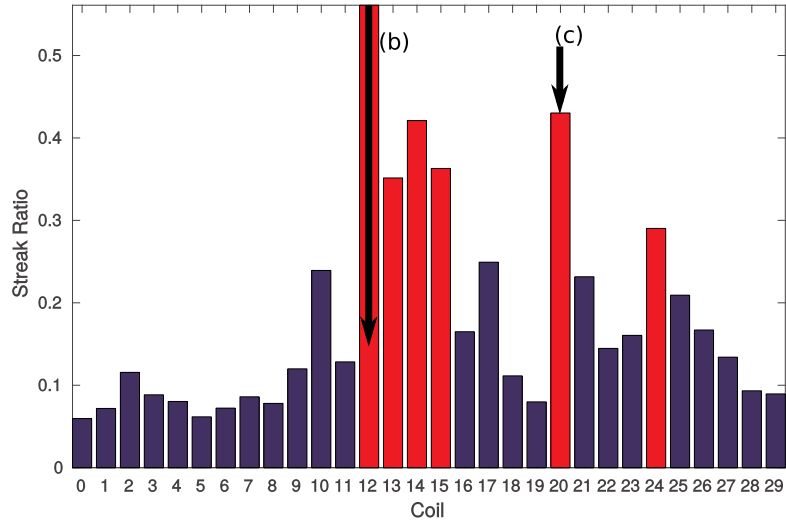
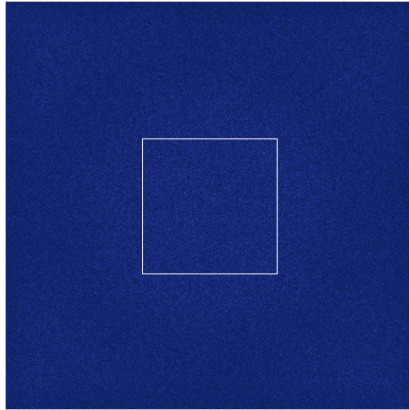


Figure 5.6: Example of calculated streak ratios of Grimm et al.’s method [28] for HEART2. (a) shows the calculated streak ratios; gridding reconstructions of the indicated coils are shown in (b) and (c).  $\tilde{R}_n$  is not a good measure for the streak content in the individual coils, since (c) is the single coil responsible for streak artifacts in the final reconstruction (see Figure 5.4).

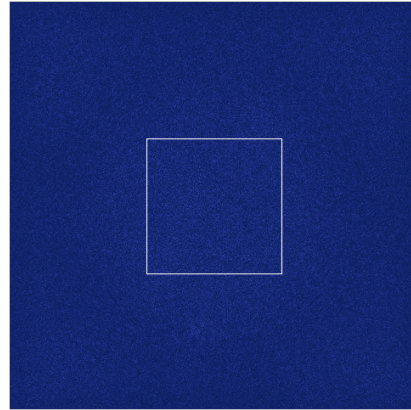
## 5. Coil Selection



(a)



(b)



(c)

Figure 5.7: Example of calculated streak ratios of Grimm et al.'s method [28] for HEART2. (a) shows the calculated streak ratios, gridding reconstructions of the indicated coils are shown in (b) and (c). High streak ratios were assigned to both coils, while neither contains useful signal.

## 5.2. Sinogram-based Selection

In order to address the shortcomings of Grimm et al.'s method [28] in the context of real-time MRI, a modified algorithm was developed on its basis. The general idea is to use sinograms to reach a compromise between the full image space information needed in Xue et al.'s [27] algorithm and the pure  $k$ -space implementation of Grimm et al. [28]. Furthermore, low intensity coils are identified and ignored so that they do not influence the streak ratio calculation. They are, however, not excluded, since the subsequent coil compression will weigh them appropriately.

The algorithm, termed sinogram-based selection, is as follows:

1. For each coil  $n$ , generate a high-pass filtered variant  $h_n$  and a low-pass filtered variant  $l_n$  of the ungridded  $k$ -space data.
2. Calculate the 1D discrete Fourier transform (DFT) along the sample direction, yielding high and low resolution sinograms  $s_{h,n}$  and  $s_{l,n}$ .
3. Approximate the signal contribution  $F_n$  of each coil to the FOV by the  $L^2$  norm of the inner part of the high resolution sinogram. The width of this inner part is the length of the diagonal of the FOV. Normalize by dividing by  $\sum_n F_n$ .
4. Calculate the mean  $\mu_F$  and the standard deviation  $\sigma_F$  of the FOV contribution  $F_n$ . Any coil with  $F_n < \frac{1}{3}(\mu_F + \sigma_F)$  is ignored for the rest of the algorithm. Renormalize  $F_n$  for each coil.
5. Calculate the magnitude of the complex difference  $s_{\text{diff},n} = |s_{h,n} - s_{l,n}|$ , its standard deviation  $\sigma_{\text{diff},n}$  and its mean  $\mu_{\text{diff},n}$ .
6. For each coil  $n$ , apply thresholding to  $s_{\text{diff},n}$  with threshold  $T = \mu_{\text{diff},n} + 4 \cdot \sigma_{\text{diff},n}$ , that means set  $s_{\text{diff},n}$  to zero where it is smaller than  $T$ , generating the thresholded  $s_{\text{diff},n}^T$ .
7. Calculate the streak ratio  $R_n$  for each coil as  $R_n = \frac{\|s_{\text{diff},n}^T\|}{\|s_{l,n}\|}$ .
8. Apply k-means to sort the streak ratios into two groups clustered around two centers.
9. If the ratio between the high and low centers is less than 2, repeat step 8 up to 100 times.

## 5. Coil Selection

10. If the combined FOV contribution of the coils in the high group is more than 20 %, exclude the coils with the highest streak ratio until 20 % excluded intensity is reached, otherwise exclude all coils in the high group.

The thresholding of the difference sinograms is done as a crude form of noise suppression: By studying the histograms (see Figure 5.8b as an example), it can be seen that low intensity pixels dominate the difference sinogram. Thresholding in the way described in step 6 can filter these pixels and thereby emphasize the important difference between the sinograms contained in few pixels. This is also the reason why sinograms are used: as shown in Figure 5.9, the spatial origin of streak artifacts can be clearly determined from the difference sinogram. In  $k$ -space, this difference is spread out over the entire space, so no useful thresholding can be done.

The center ratio is used as a criterion for deciding if the k-means algorithm managed to identify separate groups; if the center ratio is small the distance between the groups is also small. The estimation of the contribution to the FOV is also used as a safety measure: sufficient signal in the resulting images has to be guaranteed, even at the expense of remaining artifacts. 20 % has been used as compromise between allowing the algorithm freedom to exclude coils and the need to preserve signal content in the reconstructed images. It is, however, an estimate only, since the contribution of each coil is modified by channel compression and by NLINV itself. Since sinogram-based selection shares the same k-means initialization as Grimm et al.'s method [28], it is also not guaranteed to be deterministic.

Figure 5.10 shows a comparison between using all coils and the proposed selection for datasets where it worked well: comparing Figure 5.10 to Figure 5.5 shows marked improvement over Grimm et al.'s [28] selection for real-time data.

But problems remain for other datasets: In Figures 5.11a and 5.11c, the streak artifacts in the neck region are greatly reduced, but the nose region still contains significant artifacts. Similar behaviour can be seen in Figures 5.11d and 5.11f: Here, too, streak artifacts in the nose region are unaffected, while the artifacts in the neck region are only slightly reduced. Bar diagrams of the streak ratios for these datasets can be found in Appendix A.

Because of the improved image quality gained by sinogram-based selection, a C++ implementation was written and added to the preprocessor of `nlinv++` as part of this thesis. This enables online use directly on the MRI scanner.

This implementation uses the existing calibration data<sup>3</sup> which is already used to calculate the gradient delay correction values and the coil compression matrix (PCA).

---

<sup>3</sup>The raw data of the first full frame.

Coil selection is now a step before these two others, deleting coils from the calibration data if necessary. Gradient delay values and PCA matrix are then calculated on this filtered calibration data. But the raw data sent on by the datasource still contains all coils, so it is incompatible with the calculated PCA matrix. To overcome this, columns of all zeros are added to the PCA matrix. Since the matrix-matrix product between incoming raw data and the PCA matrix has to be calculated regardless of whether coil selection is used or not, this makes applying the coil selection to subsequent frames free in terms of added calculation time. So coil selection only has a cost during initial calibration of the preprocessor. This cost is, however, quite small in terms of wall-clock time: For a common dataset with 64 coils the sinogram-based selection takes less than 0.5 s. Furthermore, the overall effect is that excluding coils through coil selection is indistinguishable from not having measured these coils at all.

## 5. Coil Selection

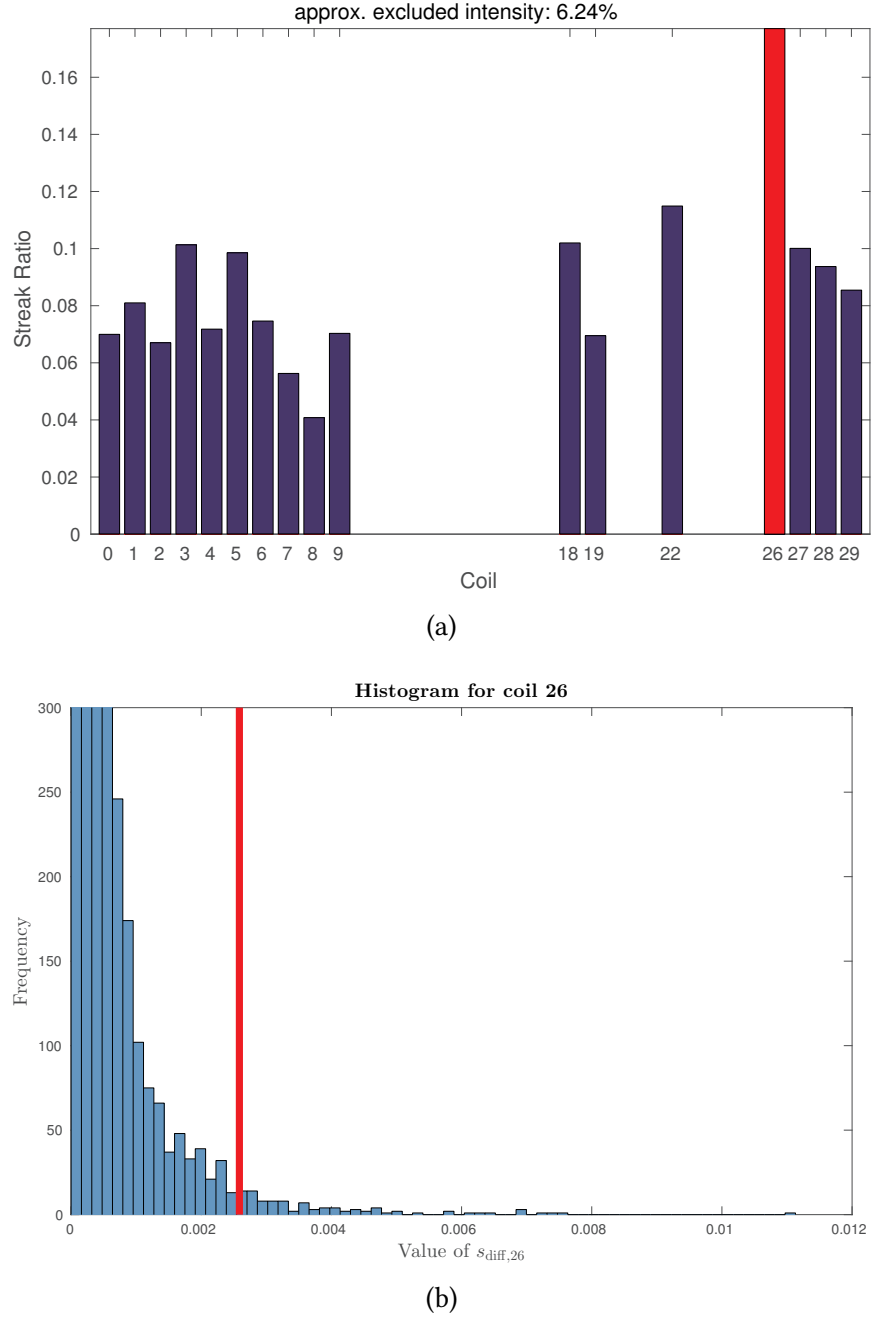


Figure 5.8: (a): Example of the calculated streak ratios using the sinogram-based selection for dataset HEART2. The coils without any streak ratio were ignored in step 4. The coil indicated in red is to be removed, which is the same coil that was removed as part of the manual selection shown in Figure 5.4. (b): Histogram of  $s_{\text{diff},n}$  for the indicated coil in (a) (see Figure 5.3d for a gridding reconstruction). The frequency axis is truncated to emphasize the small frequency values for larger values of  $s_{\text{diff},n}$ . The red vertical line indicates the threshold calculated in step 6. The value of the threshold is calculated so that the majority of the noisy low value pixels are excluded.



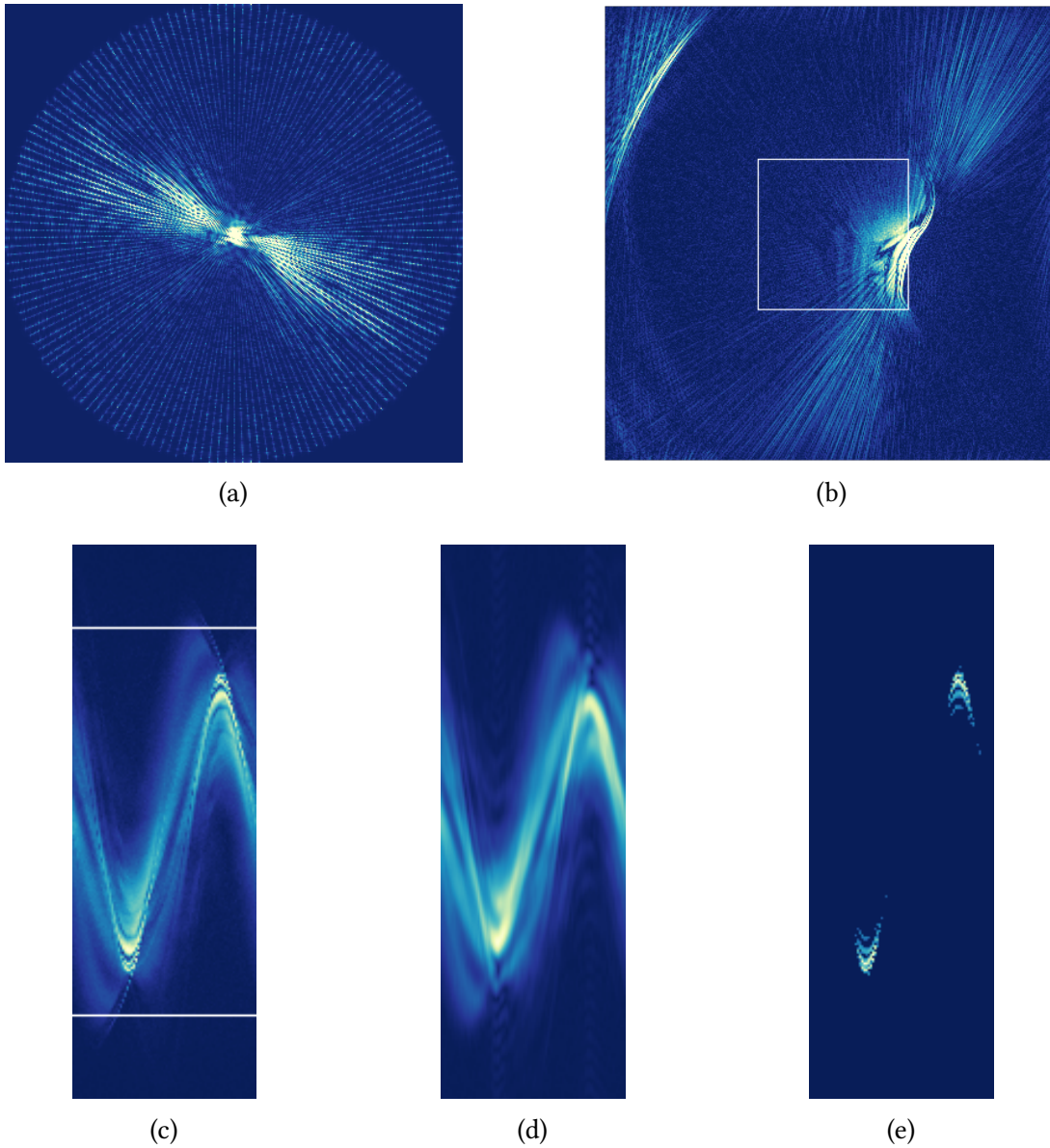


Figure 5.9: (a) Gridded  $k$ -space and (b) gridding reconstruction of the first full frame of a streaked coil removed by sinogram-based selection from dataset HEAD1 (see Figure 5.10a for an NLINV reconstruction). (c) High- and (d) low-resolution sinogram, (e) thresholded difference of sinograms for the same coil. The spatial location of the streak origin can be clearly identified in the thresholded difference of the low- and high-resolution sinograms, while it cannot be identified in the gridded  $k$ -space in (a). In (c), the area used to estimate the signal contribution to the FOV is indicated in white (see step 3).

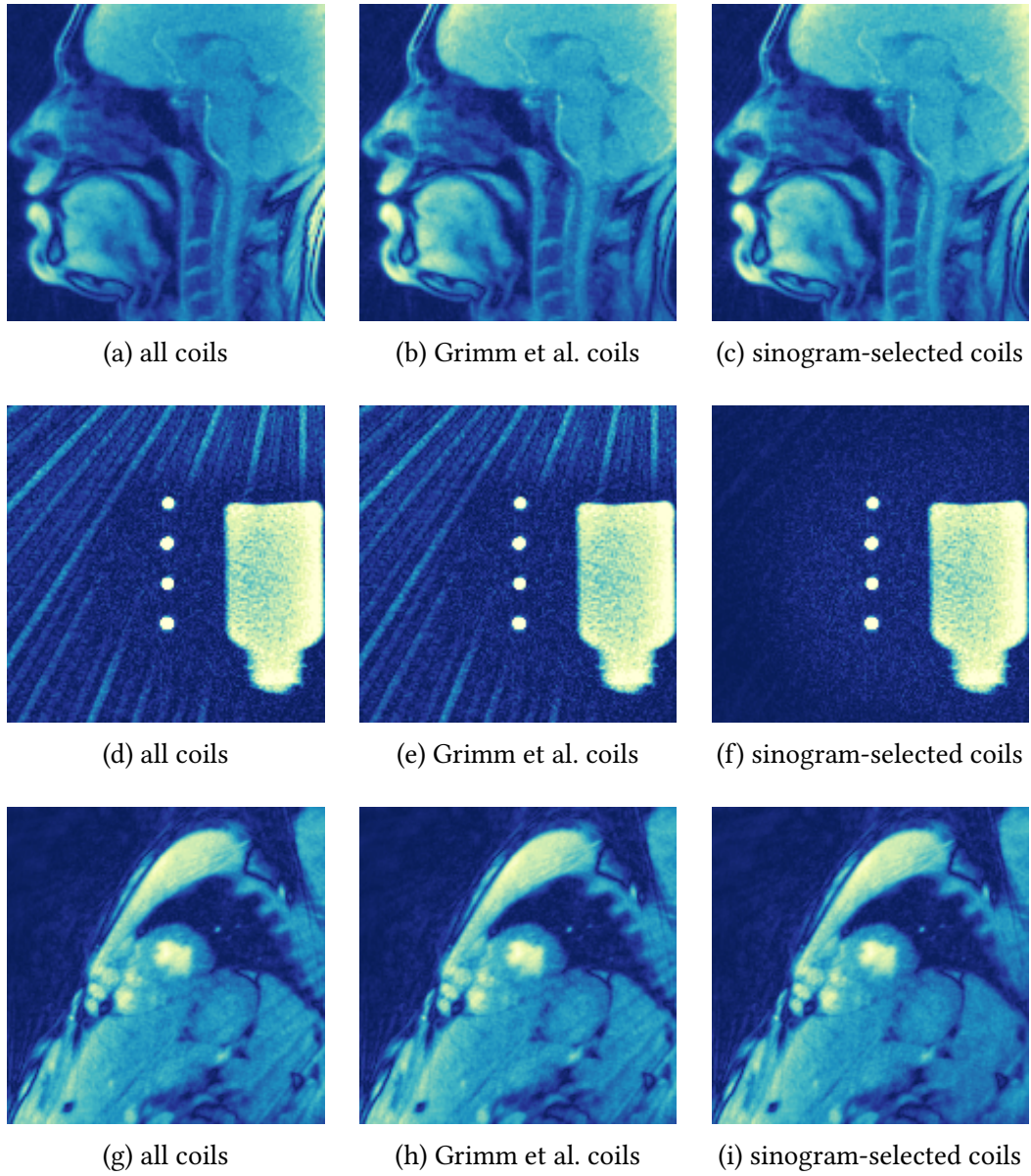


Figure 5.10: Comparison between using all coils (left column), Grimm et al.’s method [28] (center column) and the proposed sinogram-based selection (right column) for several datasets. (a) (HEAD1) shows streak artifacts in the neck region, which are greatly reduced in (c), as are the prominent streak artifacts in (d) (PHAN2) and (g) (HEART2). The artifacts in (d) and (g) are not removed by Grimm et al.’s method [28].

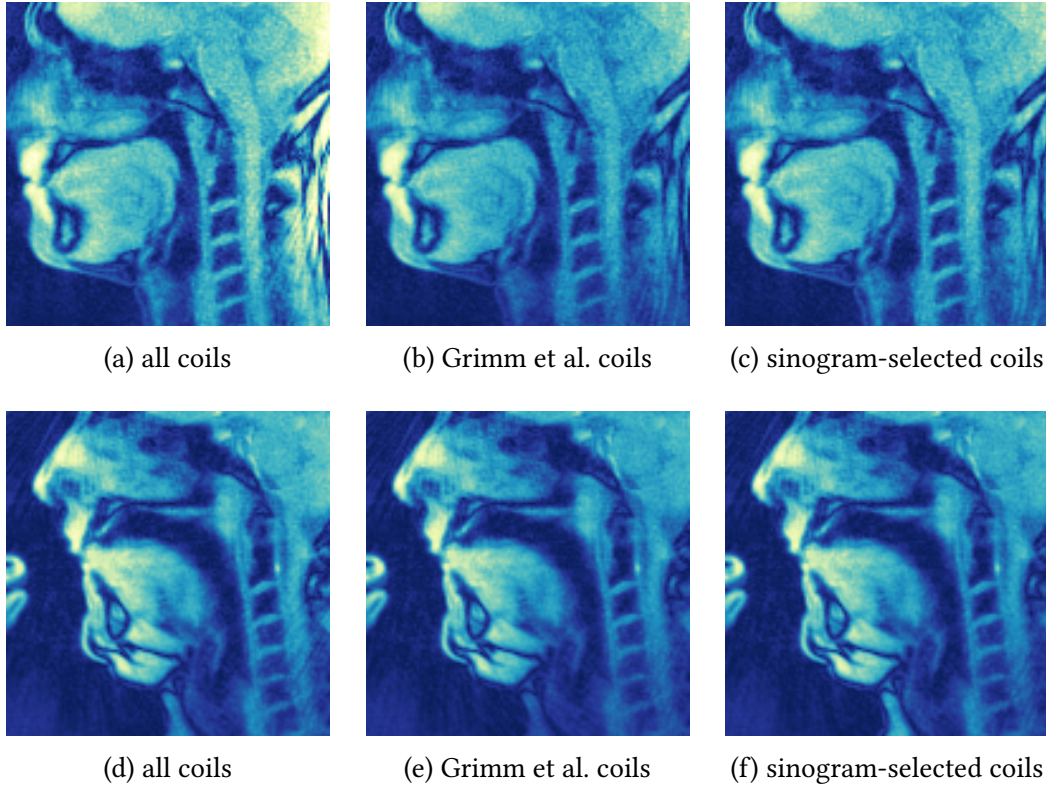


Figure 5.11: Comparison between using all coil (left column), Grimm et al.'s method [28] (center column), and the proposed sinogram-based selection (right column) for additional datasets. While both (b) and (c) (HEAD2) show reduced streak artifacts in the neck region, some artifacts are still present there. Furthermore, strong artifacts in the nose region remain unchanged compared to (a). Similarly, both (e) and (f) (HEAD4) show artifacts in the nose region of unchanged strength and only slightly reduced artifacts in the neck region compared to (d).

### 5.3. Discussion

The novel sinogram-based selection algorithm has been shown to provide better artifact-reduction than previous algorithms in the context of real-time MRI. But nontrivial problems with some datasets remain, where the streak artifact reduction is not totally satisfactory.

As Grimm et al.'s method [28], the proposed sinogram-based selection is also non-deterministic. While stable for most datasets, some datasets will show different selections on consecutive runs, leading to non-reproducible reconstructions. A further problem is the non-determined runtime: Since the k-means algorithm will try multiple times to find a selection matching all criteria, the number of tries can vary from run to run. Incidentally, the worst runtime is for datasets where no coils will be excluded: Here the maximum number of tries is exhausted, leading to longer runtimes which are still below 1 s.

In general, since the streak ratios used in both algorithms are scalars, the k-means algorithm acts as a simple threshold. Finding an appropriate threshold with which the k-means algorithm can be replaced would lead to both deterministic coil selection and runtime. But so far, no such threshold has been found.

Another possible extension is the generalization of coil selection to coil weighting: If the origin of streak artifacts are high intensity regions mostly outside of the FOV, then simply weighing the coils appropriately could lessen the severity of the artifacts while still including potentially useful signal contained in these coils. Coil selection is then simply a limiting case of coil weighting, where the coils are assigned binary weights.

And finally, regularization of the reconstruction method can be used to constrain the space of allowed solutions. So, if a method of regularization which excludes images with strong streak artifacts from the solution space could be found, it would completely negate the need for both coil selection or coil weighting methods. So far however, no methods have been found which reliably exclude streak artifacts from in-vivo acquisitions.

## 6. Summary and Outlook

In this thesis, improvements for two data preprocessing steps in real-time MRI were described, evaluated, and discussed.

Starting from the problem arising from multiple receiver coils in modern MRI, the current PCA-based compression is introduced in Chapter 4. From there, an optimized compression algorithm is described and its adaptation to real-time MRI is evaluated. This revealed difficulties with integrating the optimized combination into the current real-time MRI pipeline. Furthermore, the improvement in image quality was judged as being too small compared to these drawbacks to justify inclusion into the real-time pipeline.

Based on two existing algorithms, this thesis developed and evaluated a new algorithm for coil selection in order to reduce streak artifacts (Chapter 5). The proposed sinogram-based selection provides significant improvement over existing algorithms for real-time MRI. While still not capable of removing all streak artifacts, it does provide mitigation in a number of datasets.

Further work is necessary to identify the reasons for this incomplete artifact removal. Another area warranting further investigation is for acquisition modes other than anatomical: In phase contrast flow MRI [29], the main problem is streak artifacts in the phase map. There, coil selection approaches like the proposed sinogram-based selection do not provide a benefit (see Figure 6.1). A reason for this is the different streak origin: Here, susceptibility differences lead to phase distortions which in turn lead to streak artifacts. In Figure 6.1, the susceptibility difference is between the venous blood and the surrounding brain tissue. Since these are phase effects, magnitude-based coil selection methods are not suited for these kinds of streak artifacts and alternatives need to be explored.

In general, sinogram-based selection leads to improved image quality in a number of important acquisition schemes, including real-time MRI of the heart and head. A C++ implementation was therefore added to `nlinv++` as part of the real-time pipeline and it is currently used by default on all anatomical real-time MRI scans acquired in the institute.



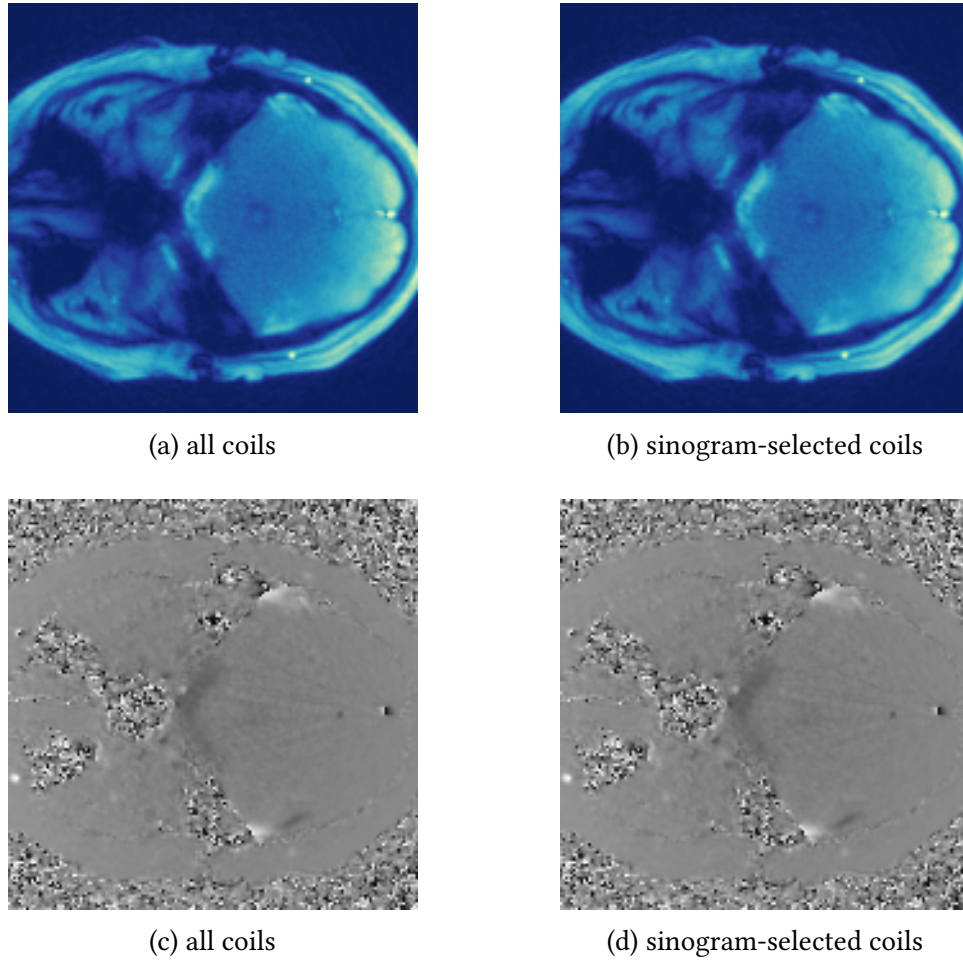


Figure 6.1: Phase-contrast flow dataset FLOW1, showing a transversal slice through the brain. (a) and (b) show the magnitude images with and without sinogram-based coil selection. Neither image contains streak artifacts. (c) and (d) show the corresponding phase difference maps, which are proportional to flow velocity perpendicular to the image plane. (c) contains streak artifacts originating from a blood vessel in the anterior region of the brain, the sagittal sinus, which are not reduced by coil selection (d). The streak ratios calculated by sinogram-based selection can be found in Figure A.5 in Appendix A.

## A. Additional Figures

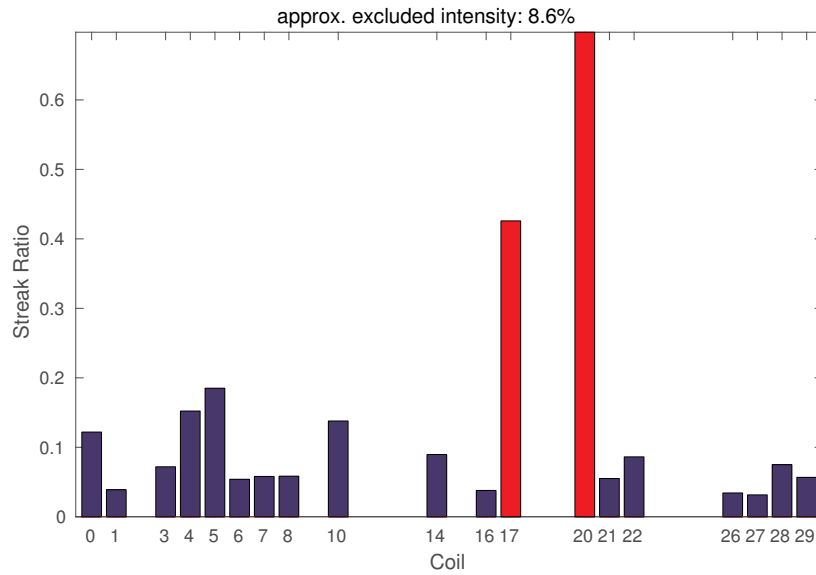


Figure A.1: Result of the sinogram-based selection for dataset PHAN1. Coils in red are to be excluded.

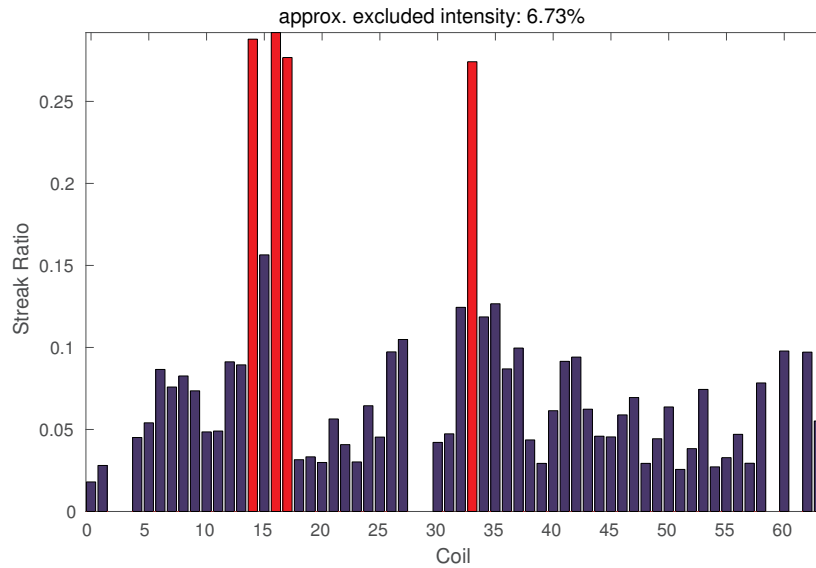


Figure A.2: Result of the sinogram-based selection for dataset HEAD1. Coils in red are to be excluded.

## A. Additional Figures

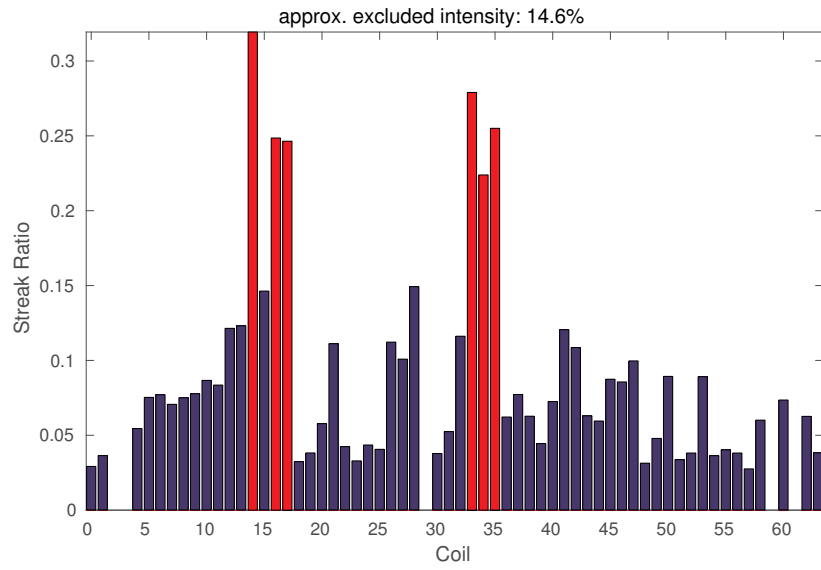


Figure A.3: Result of the sinogram-based selection for dataset HEAD2. Coils in red are to be excluded.

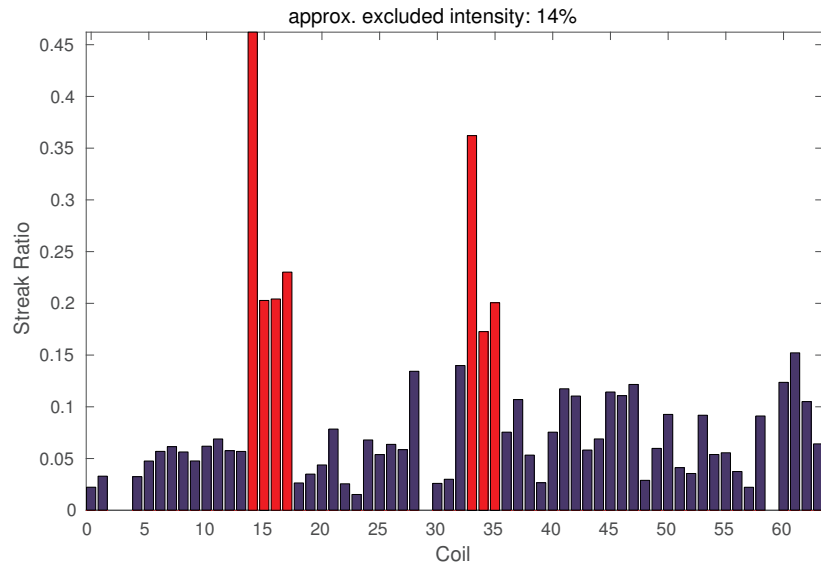


Figure A.4: Result of the sinogram-based selection for dataset HEAD4. Coils in red are to be excluded.



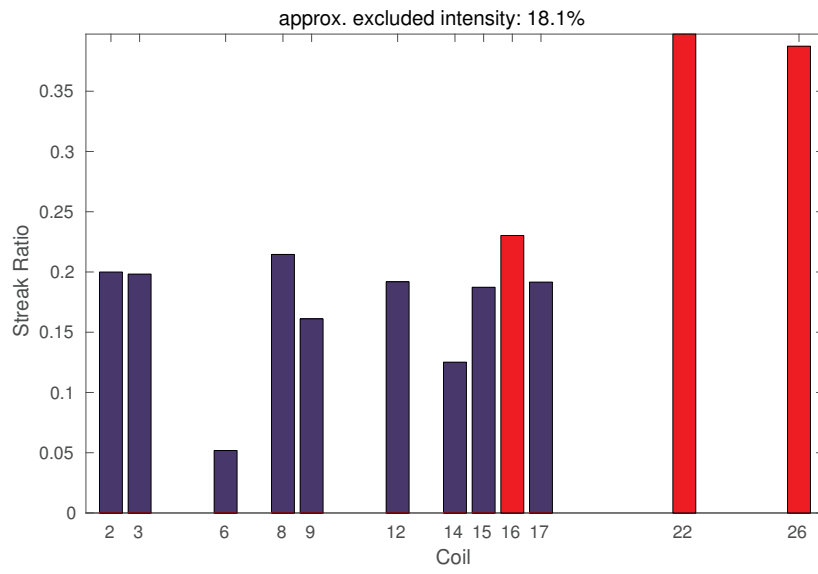


Figure A.5: Result of the sinogram-based selection for dataset FLOW1. Coils in red are to be excluded.



## B. Sequence Parameters

Table B.1: Descriptions of sequences used in this thesis.

---

PHAN1	Static commercial water phantom.
PHAN2	Perfusion phantom during active flow.
HEAD1	Midsagittal slice of the head during speaking. Human male with no known illnesses, 24 years old.
HEAD2	Midsagittal slice of the head during speaking. Human male with no known illnesses, 28 years old.
HEAD3	Midsagittal slice of the head during speaking. Human male with no known illnesses, 26 years old.
HEAD4	Midsagittal slice of the head while playing a brass instrument. Human male with no known illnesses, 48 years old.
HEAD5	Midsagittal slice of the head while playing a brass instrument. Human female with no known illnesses, 26 years old.
HEART1	Short-axis view of the heart. Human male with no known illnesses, 25 years old.
HEART2	Short-axis view of the heart. Human male with no known illnesses, 20 years old.
HEART3	Short-axis view of the heart. Human male with no known illnesses, 36 years old.
FLOW1	Phase contrast flow acquisition of a transversal slice through the brain. Human male with no known illnesses, 33 years old.

---

Table B.2: Overview over sequences parameters.

<b>Label</b>	$T_R$ [ms]	$T_E$ [ms]	$n_{\text{spokes}}$ [1]	$n_{\text{turns}}$ [1]	$\alpha$ [°]	<b>FOV</b> [mm <sup>2</sup> ]	<b>Resolution</b> [mm <sup>3</sup> ]	<b>Frame rate</b> [ $\frac{1}{s}$ ]	<b>Bandwidth</b> [ $\frac{\text{Hz}}{\text{pixel}}$ ]	<b>TNumber</b>
PHAN1	1.63	0.95	7	7	10	256×256	1.6×1.6×6	30	1955	T3506
PHAN2	2.32	1.58	17	5	8	192×192	1.2×1.2×6	25	1565	T11500
HEAD1	1.96	1.28	17	5	5	192×192	1.5×1.5×10	30	1860	T6954
HEAD2	2.02	1.28	9	7	5	192×192	1.4×1.4×8	55	1600	T16936
HEAD3	2.0	1.28	5	9	5	192×192	1.4×1.4×8	100	1670	T17086
HEAD4	1.96	1.23	17	5	5	192×192	1.5×1.5×10	30	1630	T25921
HEAD5	2.02	1.28	9	7	5	192×192	1.4×1.4×8	55	1600	T17037
HEART1	1.96	1.22	17	5	8	256×256	1.6×1.6×6	30	1565	T18907
HEART2	2.22	1.28	5	5	16	256×256	1.6×1.6×6	30	1040	T10366
HEART3	2.26	1.47	27	5	4	256×256	1.0×1.0×6	16	1395	T16228
FLOW1	5.19	4.36	13	5	10	192×192	1.2×1.2×5	7	1250	T13480

# Bibliography

- [1] P. C. Lauterbur. “Image formation by induced local interactions. Examples employing nuclear magnetic resonance”. In: *Nature* 242.5394 (1973), pp. 190–191 (cit. on p. 1).
- [2] J. Frahm et al. “Hochfrequenz-Impuls und Gradienten-Impuls-Verfahren zur Aufnahme von schnellen NMR-Tomogrammen unter Benutzung von Gradientenechos”. German pat. req. P 35 04 734.8. Max Planck Gesellschaft. 1985-02 (cit. on pp. 1, 8).
- [3] J. Frahm, A. Haase, and D. Matthaei. “Rapid NMR imaging of dynamic processes using the FLASH technique”. In: *Magnetic Resonance in Medicine* 3.2 (1986), pp. 321–327 (cit. on p. 1).
- [4] A. Haase et al. “FLASH imaging: rapid NMR imaging using low flip-angle pulses”. In: *Journal of Magnetic Resonance*. 67 (1986), pp. 258–266 (cit. on p. 1).
- [5] A. Deshmane et al. “Parallel MR imaging”. In: *Journal of Magnetic Resonance Imaging* 36.1 (2012), pp. 55–72 (cit. on pp. 1, 8).
- [6] M. Uecker et al. “Real-time MRI at a resolution of 20 ms”. In: *NMR in Biomedicine* 23.8 (2010), pp. 986–994 (cit. on pp. 1, 10).
- [7] M. A. Bernstein, K. F. King, and X. J. Zhou. *Handbook of MRI Pulse Sequences*. Elsevier Academic Press, 2004 (cit. on pp. 3, 7, 12, 16).
- [8] E. M. Haacke et al. *Magnetic Resonance Imaging: Physical Principles and Sequence Design*. Wiley, 1999 (cit. on pp. 3, 4, 6–8).
- [9] A. Hendrix. *Magnets, Spins, and Resonances – An Introduction to the basics of Magnetic Resonance*. Siemens AG Medical Solutions, 2003 (cit. on p. 4).
- [10] M. Uecker. “Nonlinear Reconstruction Methods for Parallel Magnetic Resonance Imaging”. PhD thesis. Georg-August-Universität Göttingen, 2009. URL: <http://hdl.handle.net/11858/00-1735-0000-0006-B3C6-3> (visited on 2015-12-14) (cit. on pp. 5, 9, 11, 12).

- [11] E. G. Larsson et al. “SNR-optimality of sum-of-squares reconstruction for phased-array magnetic resonance imaging”. In: *Journal of Magnetic Resonance* 163.1 (2003), pp. 121–123 (cit. on pp. 7, 36).
- [12] K. P. Pruessmann et al. “SENSE: sensitivity encoding for fast MRI”. In: *Magnetic Resonance in Medicine* 42.5 (1999), pp. 952–962 (cit. on pp. 8, 25).
- [13] M. A. Griswold et al. “Generalized autocalibrating partially parallel acquisitions (GRAPPA)”. In: *Magnetic Resonance in Medicine* 47.6 (2002), pp. 1202–1210 (cit. on p. 8).
- [14] S. Zhang, K. T. Block, and J. Frahm. “Magnetic resonance imaging in real time: advances using radial FLASH”. In: *Journal of Magnetic Resonance Imaging* 31.1 (2010), pp. 101–109 (cit. on p. 10).
- [15] M. Uecker et al. “Image reconstruction by regularized nonlinear inversion–joint estimation of coil sensitivities and image content”. In: *Magnetic Resonance in Medicine* 60.3 (2008), pp. 674–682 (cit. on pp. 11, 12).
- [16] M. Untenberger. “Multi-Echo Radial FLASH Techniques for Real-Time MRI”. PhD thesis. Otto-von-Guericke-Universität Magdeburg, 2015. URL: <http://edoc2.bibliothek.uni-halle.de/urn/urn:nbn:de:gbv:ma9:1-7052> (visited on 2016-01-04) (cit. on p. 16).
- [17] J. Klosowski and J. Frahm. “Image Denoising for Real-time MRI”. In: *Magnetic Resonance in Medicine* (2016). Submitted (cit. on p. 16).
- [18] C. J. Hardy et al. “128-channel body MRI with a flexible high-density receiver-coil array”. In: *Journal of Magnetic Resonance Imaging* 28.5 (2008), pp. 1219–1225 (cit. on p. 21).
- [19] I. T. Jolliffe. *Principal Component Analysis*. Springer Series in Statistics. Springer New York, 2006 (cit. on p. 21).
- [20] S. Zhang. “Real-Time Magnetic Resonance Imaging”. PhD thesis. Georg-August-Universität Göttingen, 2009. URL: <http://hdl.handle.net/11858/00-1735-0000-000D-F258-8> (visited on 2015-12-14) (cit. on p. 23).
- [21] M. Buehrer et al. “Array compression for MRI with large coil arrays”. In: *Magnetic Resonance in Medicine* 57.6 (2007), pp. 1131–1139 (cit. on p. 25).
- [22] D. C. Peters et al. “Undersampled projection reconstruction applied to MR angiography”. In: *Magnetic Resonance in Medicine* 43.1 (2000), pp. 91–101 (cit. on p. 37).

- [23] K. K. Vigen et al. “Undersampled projection-reconstruction imaging for time-resolved contrast-enhanced imaging”. In: *Magnetic Resonance in Medicine* 43.2 (2000), pp. 170–176 (cit. on p. 37).
- [24] G. H. Glover and D. C. Noll. “Consistent projection reconstruction (CPR) techniques for MRI”. In: *Magnetic Resonance in Medicine* 29.3 (1993), pp. 345–351 (cit. on p. 37).
- [25] D. C. Noll et al. “Magnetic resonance reconstruction from projections using half the data”. In: *Proceedings of the International Society for Optical Engineering*. Vol. 1443. 1991, pp. 29–36 (cit. on p. 37).
- [26] J. Du et al. “Artifact reduction in undersampled projection reconstruction MRI of the peripheral vessels using selective excitation”. In: *Magnetic Resonance in Medicine* 51.5 (2004), pp. 1071–1076 (cit. on p. 37).
- [27] Y. Xue et al. “Automatic coil selection for streak artifact reduction in radial MRI”. In: *Magnetic Resonance in Medicine* 67.2 (2012), pp. 470–476 (cit. on pp. 41, 42, 47).
- [28] R. Grimm et al. “Fast Automatic Coil Selection for Radial Stack-of-stars GRE Imaging”. In: *Proceedings of the International Society for Magnetic Resonance in Medicine*. Ed. by G. E. Gold. Salt Lake City, Utah, USA, 2013 (cit. on pp. 42–48, 52–54).
- [29] A. A. Joseph et al. “Real-time phase-contrast MRI of cardiovascular blood flow using undersampled radial fast low-angle shot and nonlinear inverse reconstruction”. In: *NMR in Biomedicine* 25.7 (2012), pp. 917–924 (cit. on p. 55).





# Acknowledgements

First, I would like to thank Prof. Dr. Jens Frahm for the excellent supervision during this thesis and for giving me the opportunity to pursue my research in such a distinguished environment.

I would also like to thank Prof. Dr. Tim Salditt for reviewing this thesis as second referee.

Furthermore, I would like to thank my colleagues at the BiomedNMR, for providing an engaging and thoroughly cooperative atmosphere, and for the many helpful discussions during my thesis. Here, I would particularly like to thank Volkert Roeloffs, Dr. Dirk Voit, Zhengguo Tan, Jakob Klosowski, Dr. Oleksandr Kalentev, and Sebastian Schätz.

I am deeply indebted to Christina Bömer and Marie Zeiß for their unwavering emotional support and encouragement.

I would like to thank Prof. Dr. Thomas Pruschke for providng the  $\LaTeX$  template used to write this thesis.

**Erklärung**

nach §17(9) der Prüfungsordnung vom 05.10.2012 für den Bachelor-Studiengang Physik und den Master-Studiengang Physik an der Universität Göttingen:

Hiermit erkläre ich, dass ich diese Abschlussarbeit selbständig verfasst habe, keine anderen als die angegebenen Quellen und Hilfsmittel benutzt habe und alle Stellen, die wörtlich oder sinngemäß aus veröffentlichten Schriften entnommen wurden, als solche kenntlich gemacht habe.

Darüberhinaus erkläre ich, dass diese Abschlussarbeit nicht, auch nicht auszugsweise, im Rahmen einer nichtbestandenenen Prüfung an dieser oder einer anderen Hochschule eingereicht wurde.

Göttingen, den 17. Februar 2016

(Hans Christian Martin Holme)